Ph.D thesis

Star cluster formation and molecular cloud destruction caused by radiative feedback

Mutsuko Inoguchi
Department of Astrophysics, Faculty of Science, Kyoto University

Abstract

Understanding the star formation process is one of the most fundamental issues in astrophysics. In this thesis, we focus on the issues related to star cluster formation in molecular clouds.

An important unsolved problem in star formation theory is what determines the star formation efficiency of molecular clouds. The star formation in molecular clouds is known to be inefficient. The ionizing EUV radiation ($h\nu \geq 13.6$ eV) from young clusters has been considered as a primary feedback effect to limit the star formation efficiency (SFE). We here focus on effects of the stellar FUV radiation (6 eV $\leq h\nu \leq$ 13.6 eV) during the cloud disruption stage. The FUV radiation may further reduce the SFE via photoelectric heating, and it also affects the chemical states of the gas that is not converted to stars ("cloud remnants") via photodissociation of molecules. We have developed a one-dimensional semi-analytic model which follows the evolution of both the thermal and chemical structure of a photodissociation region (PDR) during the dynamical expansion of an H II region. We investigate how the FUV feedback limits the SFE, supposing that the star formation is quenched in the PDR where the temperature is above a threshold value (e.g., 100K). Our model predicts that the FUV feedback contributes to reduce the SFEs for the massive ($M_{\rm cl} \gtrsim 10^5\ M_\odot$) clouds with the low surface densities ($\Sigma_{\rm cl} \lesssim 100\ {\rm M_\odot pc^{-2}}$). Moreover, we show that a large part of the H_2 molecular gas contained in the cloud remnants should be "CO-dark" under the FUV feedback for a wide range of cloud properties. Therefore, the dispersed molecular clouds are potential factories of the CO-dark gas, which returns into the cycle of the interstellar medium (Chapter 2).

Although our 1D semi-analytic model can explain the SFE of molecular clouds, there are some unrealistic assumptions to simplify the calculation. Therefore, for more realistic model, numerical 3D radiation hydrodynamics (RHD) simulations and synthetic observation are required. Fukushima & Yajima (2021) studied the formation of young massive star clusters (YMCs) by performing 3D RHD simulations including both EUV and FUV radiation. Then we discussed the observational signatures of the molecular clouds during the formation of the YMCs based on the results of their simulation. We calculated and compared the intensity distributions of emission lines such as [C II] and [O I] and the line-of-sight motion of the molecular gas on the near side of the cluster from the results of the two simulations where YMC forms or not. The main difference between the two models is whether or not active star formation persists after 1.5 free-fall time. As a result, the infall motion of molecular gas toward the ionized region and very strong centralized emission lines such as [C II] are found to be the observational signatures of YMC formation (Chapter 3).

Contents

Chapter 1

Introduction

Star formation is one of the most critical issues in astrophysics. In fact, the evolution of galaxies is largely influenced by the star formation activities. There are many unresolved problems, however, in star formation processes. In this thesis, we focus on the issues related to star cluster formation in molecular clouds.

1.1 Molecular cloud destruction by FUV feedback

The evolution of galaxies is closely related to the star formation activities. In nearby galaxies, the overall star formation rate is quite low; the cold molecular gas is converted to stars in a slow pace. The resulting depletion timescale of the molecular gas is $\sim$ Gyr over the galactic scale (e.g., Kennicutt & Evans 2012). By contrast, the star formation occurs in the much shorter timescale over the small ($\lesssim 100$ pc) cloud scales (e.g. Lee et al. 2016). The lifetime of an individual giant molecular cloud (GMC) is estimated to be less than $\sim 10-30$ Myr (e.g., Fukui & Kawamura 2010). A possible explanation for the above observations is that only a small fraction of the gas is used to form stars in each cloud. Physical processes responsible for such a low star formation efficiency (SFE) are yet to be fully clarified.

A promising process to limit the SFE is the so-called "stellar feedback", i.e., radiative and kinetic energy injection from stars into natal clouds (e.g. Dale 2015; Naab & Ostriker 2017; Krumholz et al. 2019). The SFEs are lowered if the clouds are promptly destroyed by the feedback before a large part of the gas turns into stars. Recent studies show that such an evolution is caused indeed by the feedback from high-mass stars in GMCs (e.g., Kruijssen et al. 2019, see Fig. 1.1). It is further suggested that the cloud destruction advances over only a few Myrs, which is shorter than the stellar lifetime. Therefore, radiation-driven or wind-driven bubbles expanding around high-mass stars before the first supernova explosion are believed to play an important role in GMC destruction.

H II regions created by the stellar ionizing (EUV; $h\nu \geq 13.6$ eV) radiation cause the dynamical bubble expansion in GMCs (e.g., Yorke 1986). Since the expansion speed is supersonic with respect to the surrounding cold medium, the H II bubble expands driving a preceding shock front. The shocked gas is taken into a shell around the H II region, which continues to expand sweeping up the surrounding medium into the shell. While the gas dynamics varies depending on density structure of the clouds (e.g., Franco et al. 1990),

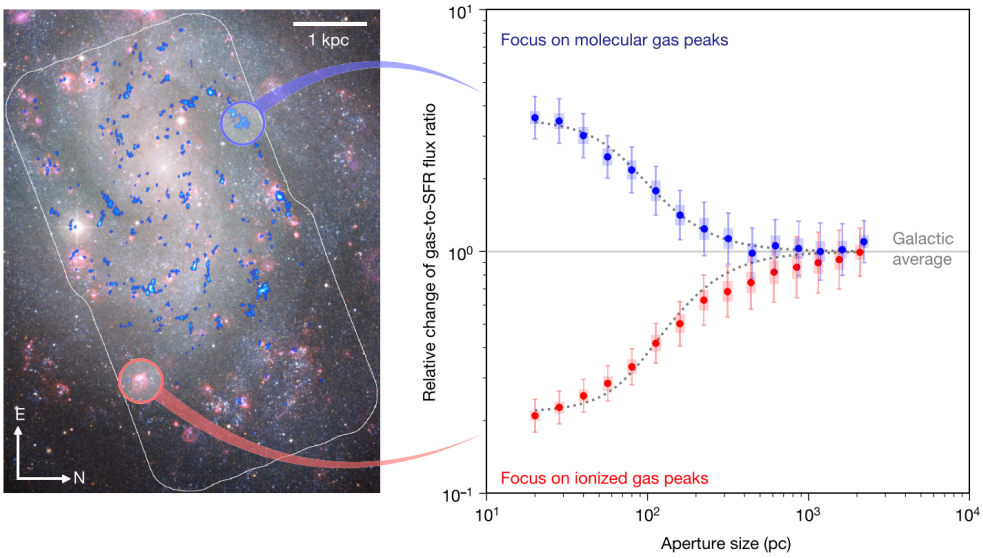

Figure 1.1: De-correlation of molecular gas and young stellar emission on sub-kiloparsec scale (Kruijssen et al. 2019). *Left panel:* Optical composite images of NGC 300 overlaid with ALMA image of CO(1-0) emission (blue). Pink color indicates H α emissions, tracing the young stars. *Right panel:* CO-to-Hα ratio relative to the galactic average as a function of aperture size. Blue points represent the ratio of CO-emission region, while red points represent the same of Hα-emission region. One cannot distinguish them for larger aperture size, whereas the symmetric de-correlation is clear for smaller size ($\lesssim$ 150 pc).

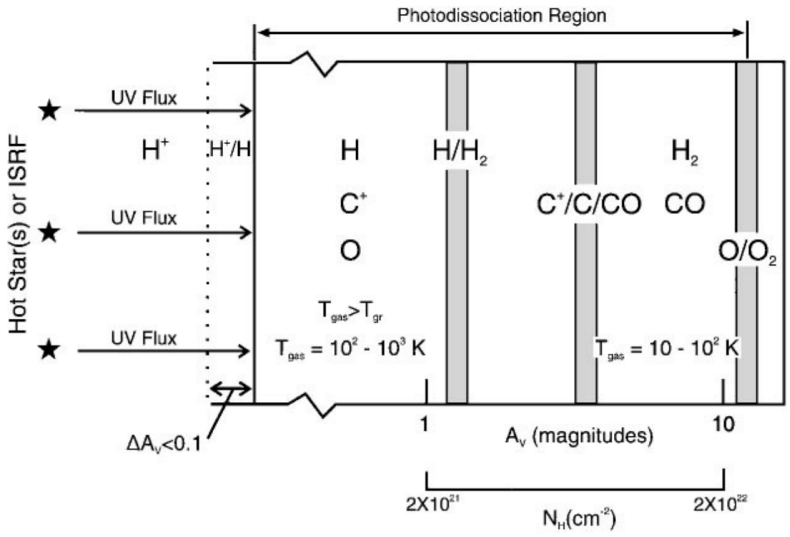

Figure 1.2: A schematic diagram of a photodissociation region (Hollenbach & Tielens 1999).

theoretical studies have suggested that the resulting EUV feedback operates to limit the SFE (e.g. Whitworth 1979; Williams & McKee 1997; Matzner 2002; Kim et al. 2016). In recent years, a number of authors have conducted radiation-hydrodynamics numerical simulations that directly follow the EUV feedback in GMCs that are filled with turbulence in reality (e.g., Mellema et al. 2006; Dale et al. 2012; Geen et al. 2015; Howard et al. 2016; Gavagnin et al. 2017; Kim et al. 2018; Haid et al. 2019; He et al. 2019; González-Samaniego & Vazquez-Semadeni 2020). Overall, these studies have confirmed that the EUV feedback lowers the SFEs, though its impact depends on cloud properties such as the mass and surface density.

There are extensive studies regarding the ionizing radiation feedback that have been performed. In fact, however, the dissociating radiation (FUV; 6.0 eV $\leq h\nu \leq$ 13.6 eV) as well as ionizing radiation is emitted from young star clusters. Many studies have investigated the dynamical effect of the radiation pressure of the FUV radiation. Indeed, some of them shows that the feedback caused by the radiation force contributes to regulating the star formation in GMCs, although the resulting SFE is a bit higher than what observations suggest (e.g., Thompson & Krumholz 2016; Raskutti et al. 2016, 2017; Kim et al. 2018).

Whereas the radiation pressure force is one dynamical aspect of the FUV feedback, we in this paper consider the other aspect of the thermal and chemical FUV feedback on GMCs. Hereafter we use the terms of the EUV feedback and FUV feedback to designate the dynamical effects caused by H II regions and thermal and chemical effects caused by photodissociation region (PDRs), respectively. The FUV radiation creates a PDR, where the gas is heated up via photoelectric effect, around an H II region (e.g., Hollenbach & Tielens 1999, see Fig. 1.2). The local Jeans mass is enhanced by such additional heating, which prevents the gravitational collapse of dense cores. As a result, the FUV radiation may further contribute to the reduction of the SFEs in GMCs (e.g., Roger & Dewdney 1992; Diaz-Miller et al. 1998; Inutsuka et al. 2015). For example, Forbes et al. (2016) shows that the photoelectric heating plays the dominant role on determining the star formation rate in dwarf galaxies ($\sim$ kpc-scale) rather than other feedback effects (but see also Hu et al. 2017). In the same vein, Peters et al. (2017) and Butler et al. (2017) have incorporated the FUV feedback in simulations following the star formation in a $\sim$ kpc-scale region of the Galactic disk, concluding that it is necessary to explain the observed depletion timescale of $\sim$ Gyr. On the individual GMC scale ($\lesssim$ 100 pc), by contrast, the effects of FUV feedback has not been fully investigated yet.

The low SFE means that most of the GMC gas is returned into the cycle of the interstellar medium, without being turned into stars. A part of such a "remnant" gas may be recycled for the subsequent GMC formation. The stellar FUV radiation also substantially affects the physical and chemical states of the cloud remnants. Since the FUV radiation destroys molecules via photodissociation, it generally creates cold H_2 gas associated with little amount of CO molecules (e.g., van Dishoeck & Black 1988; Wolfire et al. 2010). Since such gas is difficult to be observed via CO emission, it is called as "CO-dark" (van Dishoeck 1992). Recent observations via γ-ray (Grenier et al. 2005), dust continuum (Planck Collaboration et al. 2011), and C^+ line emission (Pineda et al. 2013, 2014) suggest the existence of the CO-dark gas, and no less than $\sim 30 - 70$ % of the molecular gas is actually CO dark in our Galaxy. Theoretical studies also support such Galactic-scale observations (e.g. Smith et al. 2014; Gong et al. 2018). On the cloud scale, the appearance of the CO-dark gas during

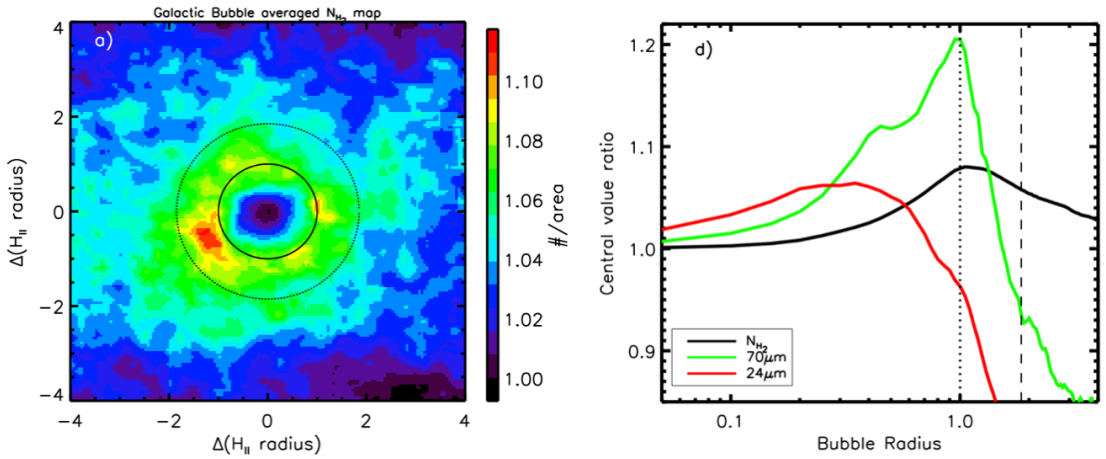

Figure 1.3: Averaged properties of observed Galactic shells around bubbles (Palmeirim et al. 2017). *Left panel:* averaged column density distribution around the bubbles. The color scaling represents the column density relative to the value at the bubble center. *Right panel:* Circularly averaged profiles of the column density (black), infrared emission at the wavelengths of 70 μm (green) and 24 μm (red). The vertical dotted and dashed lines correspond to the radii indicated in the left panel.

the formation of molecular clouds has been suggested (e.g., Clark et al. 2012). However, the CO-dark gas phase while the clouds are being dispersed is yet to be further studied (e.g., Hosokawa & Inutsuka 2007; Gaches & Offner 2018; Seifried et al. 2019).

As seen above the stellar FUV radiation should cause the additional feedback that affects the SFEs and chemical compositions of the cloud remnants. Whereas fully considering such effects requires expensive numerical simulations of radiation-magneto-hydrodynamics, we here adopt a one-dimensional semi-analytic treatment that guides our understanding. Kim et al. (2016) have developed a semi-analytic model for expansion of an H II region driven by photoionization and radiation pressure. The minimum SFEs limited by the EUV feedback have been evaluated as functions of the cloud masses and surface densities. However, they ignore the roles of the FUV feedback. Hence we construct a new model based on Kim et al. (2016), where both the FUV and EUV feedback effects are included. In order to evaluate the FUV feedback, we solve the thermal and chemical structure of PDRs around H II regions assuming the spherical symmetry. Although simple, this approach allows us to consider impacts of the FUV feedback against a variety of GMCs having different properties. We first investigate how much the FUV feedback contributes to reducing the SFEs. Next we consider the chemical compositions of the GMC remnants under the FUV feedback, showing that they are potential factories of the CO-dark molecular gas.

Recent infrared observations have reported numerous shell-like structure in our Galaxy (e.g., Palmeirim et al. 2017, see Fig. 1.3). Such a large sample should contain H_2 molecular shells created around massive stars. We finally compare the 1D semi-analytic models to statistical samples of Galactic bubbles and associated shells provided by recent observations (see Chapter 2).

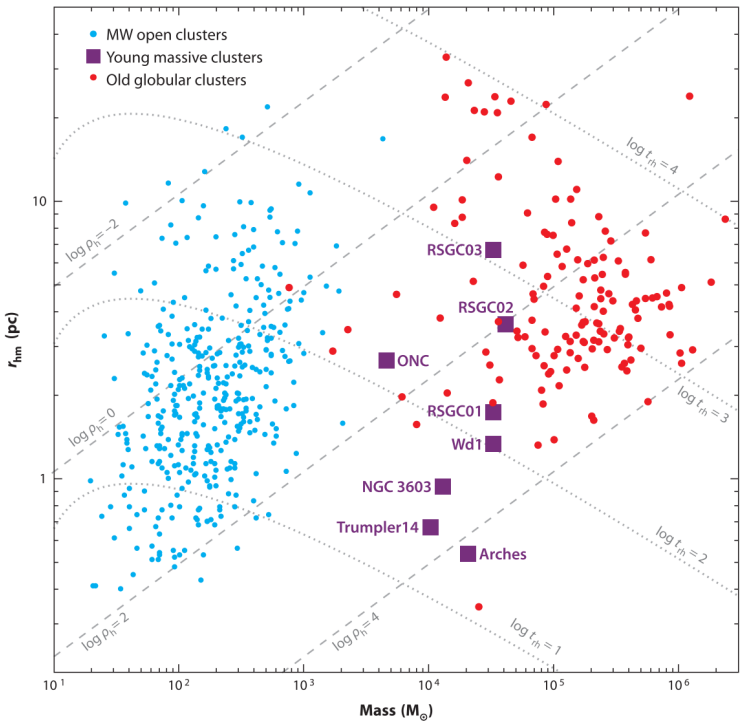

Figure 1.4: Radius-mass diagram of star clusters (Portegies Zwart et al. 2010). Each symbol shows open clusters in our Galaxy (blue dots), young massive clusters in the Local Group (purple square), and globular clusters (red dots), respectively.

1.2 Observational signatures and realistic modeling of star cluster formation

Real GMCs have inhomogeneous internal structures filled with supersonic turbulence. Accordingly, the star-cluster formation process is not so simple nor straightforward. In fact, there is great diversity in the populations of star clusters. Most of the star clusters observed in our Galaxy are so-called "open clusters (OCs)". Their typical mass is $\lesssim 10^3$ $M_\odot$ and internal density is $\lesssim 10^3$ $M_\odot$ pc^{-3}. On the other hand, the globular clusters (GCs), distributed in the Galactic halo, have quite different properties from those of OCs. GCs are very old ($\gtrsim 10$ Gyr), massive ($\gtrsim 10^5$ $M_\odot$), and dense ($\gtrsim 10^3$ $M_\odot$ pc^{-3}). The formation process of GCs is unclear, but there are some observations of young clusters which have similar properties to GCs in extragalactic starburst galaxies, so-called "young massive clusters (YMCs)". Their typical mass ($\gtrsim 10^4$ $M_\odot$) and density ($\gtrsim 10^3$ $M_\odot$ pc^{-3}) are much larger than those of OCs (Portegies Zwart et al. 2010, see Fig. 1.4). Star clusters in their early evolutionary stage are called as "embedded clusters" (Lada & Lada 2003). They are observed only with infrared light but optically invisible because of the large dust extinction. Some observations have directly detected the gas dynamics associated with the star cluster formation. For example, Sollins et al. (2005) reported the infall motion of molecular gas toward a growing star cluster. They make use of the absorption lines of NH_3 molecules against the radio continuum emission from a compact H II region (See Fig. 1.5). Therefore, for more realistic model,

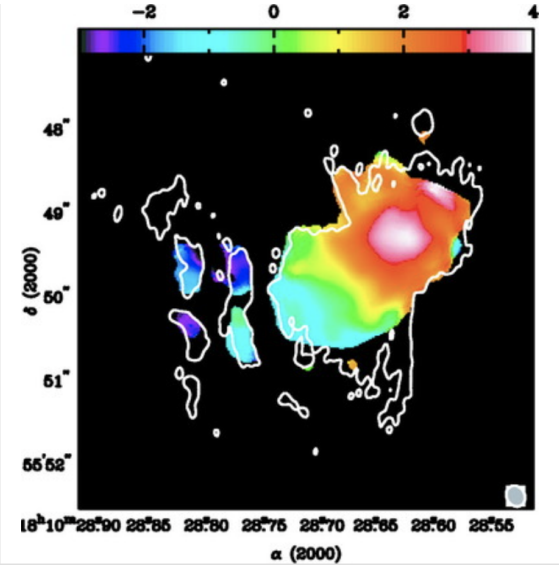

Figure 1.5: The map of the first moment of the main hyperfine component of the NH_3 (3, 3) line at ultracompact H II region G10.6-0.4 (Sollins et al. 2005). The contour is plotted from 1.3 cm continuum observation.

numerical 3D radiation hydrodynamics (RHD) simulations and synthetic observations are required for understanding the formation processes of star clusters.

Recently, such realistic modeling of the star cluster formation and destruction of the molecular clouds is becoming feasible. For instance, Fukushima & Yajima (2021) performed 3D RHD simulations to investigate the conditions for the formation of YMCs. They showed that the star clusters massive and gravitationally bound as YMCs form in massive ($\sim 10^6$ $M_\odot$) and dense (surface density $\gtrsim 300$ $M_\odot pc^{-2}$) clouds. Fig. 1.6 shows the time evolution of the cloud with mass $M_{\rm cl} = 10^6$ $M_\odot$ and radius $R_{\rm cl} = 20$ pc. In the early phase, the turbulent motion controls the gas dynamics and induces the formation of the filamentary structures in which stars form. Yet, most newborn stars distribute near the cloud center and are tightly bound at $t \sim 1.3\ t_{\rm ff}$. The star cluster at the center remains compact until the end of the simulation. On the other hand, however, in a diffuse cloud with mass $M_{\rm cl} = 10^6$ $M_\odot$ and radius $R_{\rm cl} = 40$ pc (shown in Fig. 1.7), the stellar distribution is more extended, not concentrated at the center, unlike the compact case. As the stellar mass increases, the gas is evacuated due to the radiative feedback caused by an expanding H II region.

The conditions of the stellar core formation are determined by the competition between the gravitational force and the radiative feedback. In Fig. 1.8, they show the spatial distributions of the ratio of thermal pressure ($f_{\rm p}$) to the gravitational force ($f_{\rm gr}$) in the models at $t \sim 1.3\ t_{\rm ff}$. In the case with $(M_{\rm cl}, R_{\rm cl}) = (10^6\ M_\odot,\ 20\ {\rm pc})$, the gravitational force overcomes thermal pressure in the high-density regions around the core. Thus, the high-density gas remains in the central region, and the star formation proceeds rapidly. In the case with $(M_{\rm cl}, R_{\rm cl}) = (10^6\ M_\odot,\ 40\ {\rm pc})$, however, the force from the thermal pressure is larger than the gravitational force even in the higher-density region. Therefore, the gas around the star cluster is dispersed rapidly. As a result, no stellar core is formed, and stars are widely distributed.

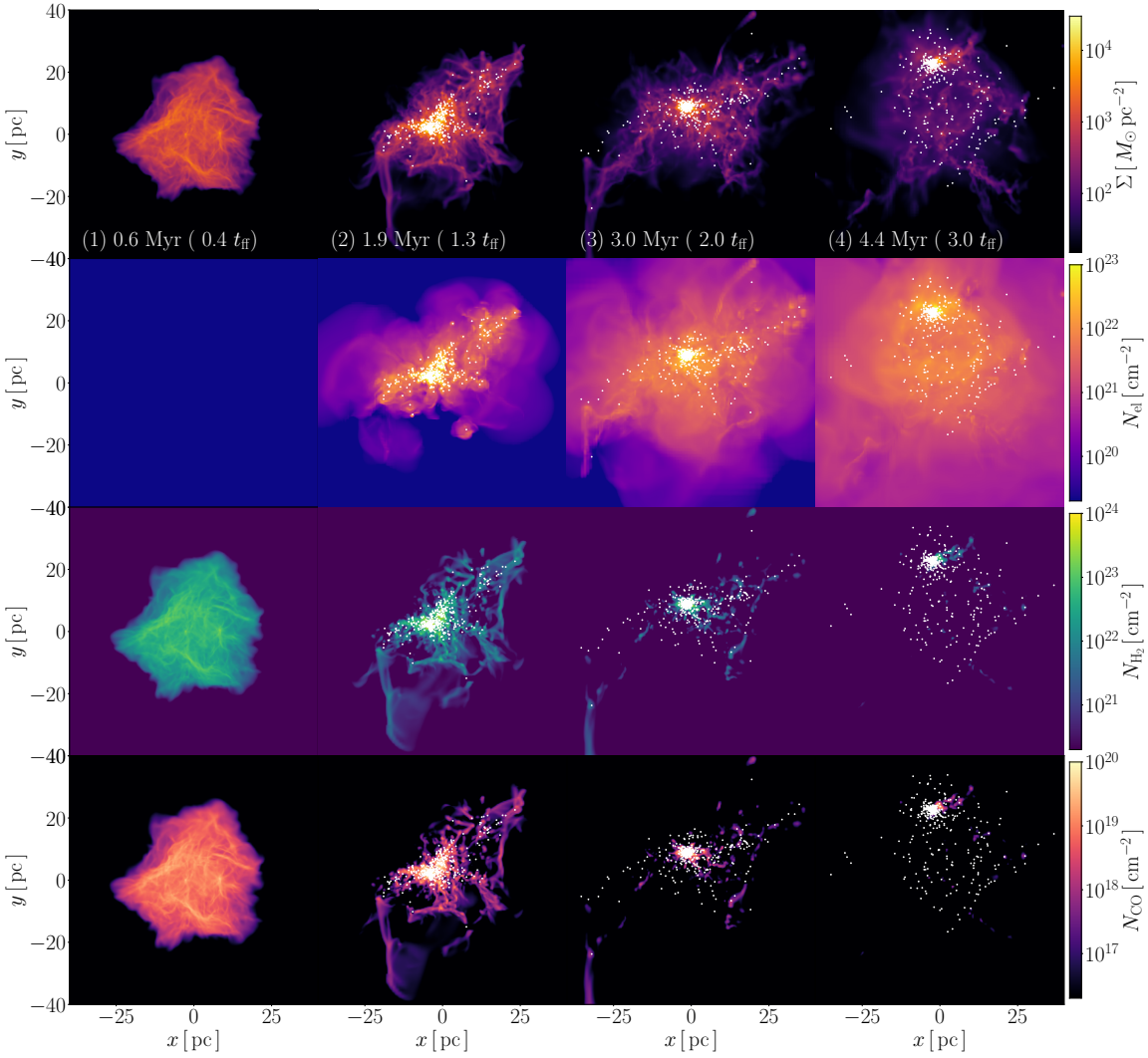

Figure 1.6: The structure of a cloud with ($M_{\rm cl}$, $R_{\rm cl}$, Z) = (10^6 M$_\odot$, 20 pc, $Z_\odot$) at t = 0.6 (0.4 $t_{\rm ff}$), 1.9(1.3 $t_{\rm ff}$), 2.9(2 $t_{\rm ff}$) and 4.4 Myr(3 $t_{\rm ff}$). Each panel shows the surface density of gas, the number column densities of electron, H_2 and CO molecules from top to bottom. Stellar particles are shown as white dots (Fukushima & Yajima 2021).

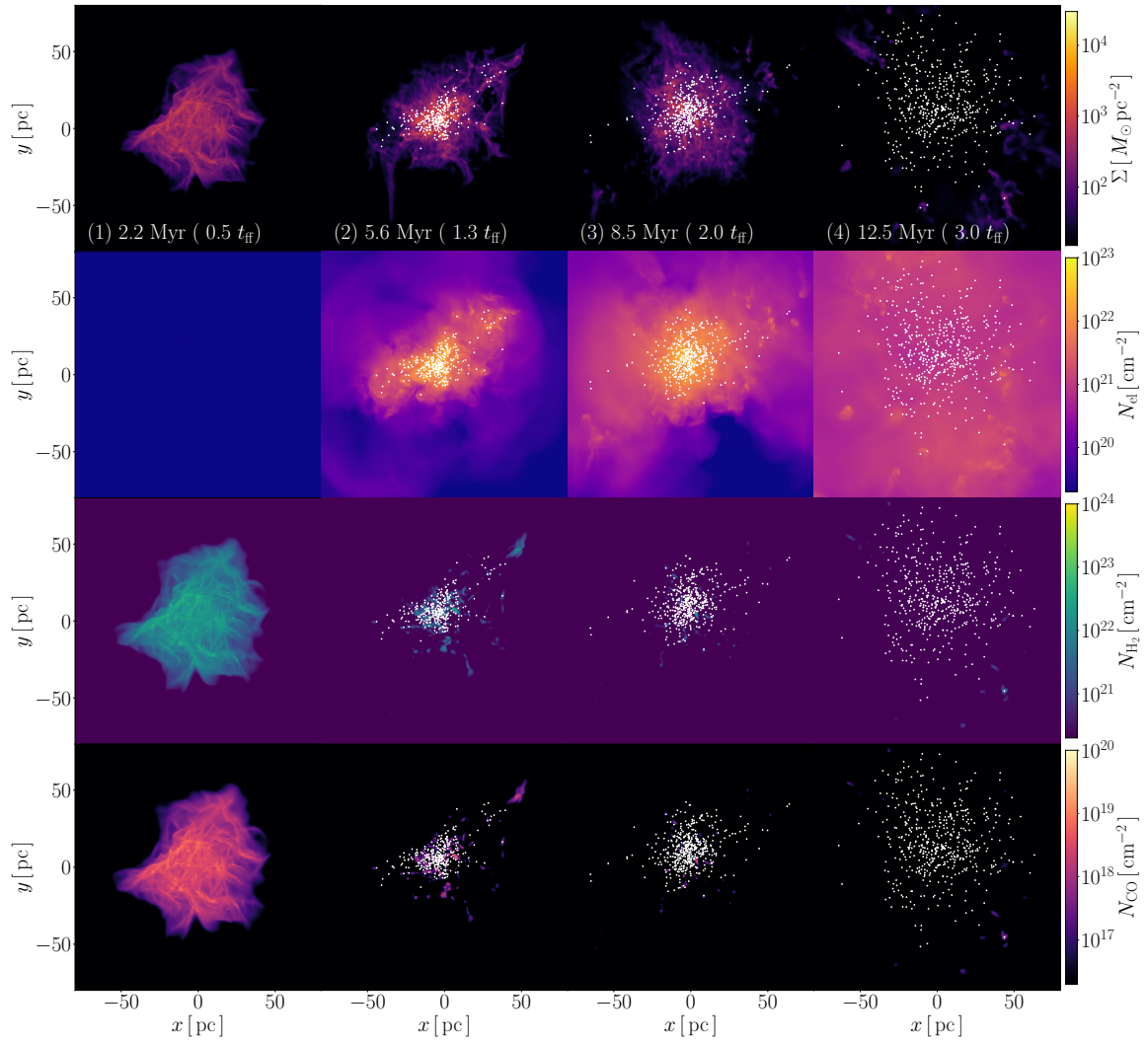

Figure 1.7: Same as Fig. 1.6, but for the case with ($M_{\rm cl}$, $R_{\rm cl}$, Z) = (10^6 M$_\odot$, 40 pc, $Z_\odot$) at t = 1.7 (0.4 $t_{\rm ff}$), 5.7 (1.3 $t_{\rm ff}$), 8.5 (2 $t_{\rm ff}$) and 12.4 Myr (3 $t_{\rm ff}$) (Fukushima & Yajima 2021).

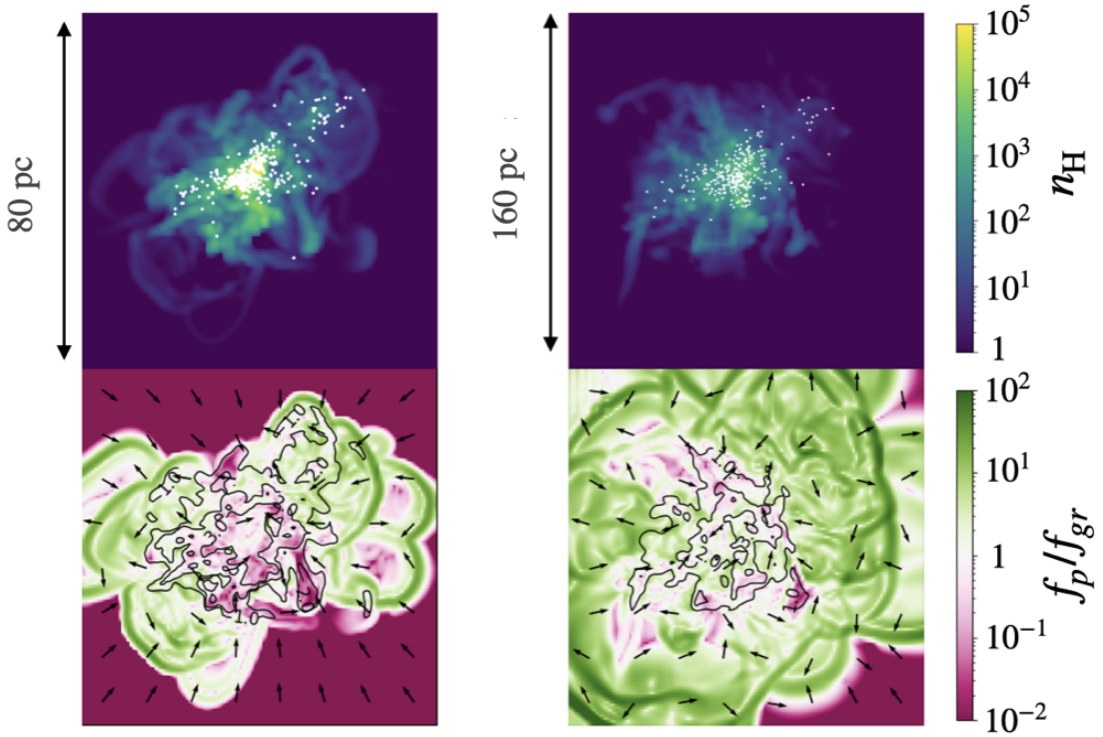

Figure 1.8: The ratio of gas pressure ($f_{\rm p}$) to the gravitational force ($f_{\rm gr}$) on the plane crossing the center of mass of the star clusters at $t \sim 1.3 t_{\rm ff}$. Each panel shows the number density of hydrogen ($n_{\rm H}$) and $f_{\rm p}/f_{\rm gr}$. Each figure shows the cases with models of ($M_{\rm cl}$, $R_{\rm cl}$, Z) = (10^6 M$_\odot$, 20 pc, $Z_\odot$) (left) and ($M_{\rm cl}$, $R_{\rm cl}$, Z) = (10^6 M$_\odot$, 40 pc, $Z_\odot$) (right) (Fukushima & Yajima 2021).

As mentioned above, the multi-dimensional simulation studies of star-cluster formation are now extensively performed, but the link to the observations need to be investigated. This is what we aim at in this thesis (see Chapter 3).

1.3 Structure of this thesis

This thesis is composed of three chapters: Chapter 2 (Molecular clouds under FUV feedback), Chapter 3 (Observational signatures of massive star-cluster forming regions), and Chapter 4 (Conclusion).

In Chapter 2, we first present our models in Section 2.1, where we outline the overall methodology in Section 2.1.1 and describe how to couple the dynamics and the thermal and chemical processes operating in the PDR in Sections 2.1.3 and 2.1.4. In Section 2.2 we show our main results. First we present a representative case of the time evolution of the thermal and chemical structure in the PDR in Section 2.2.1. Then we study the effects of the FUV feedback on limiting the SFE in Section 2.2.2, and possible chemical compositions of the cloud remnants in Section 2.2.3. We provide the relevant discussion in Sections 2.3. Most of the contents of Chapter 2 has already been published in Inoguchi et al. (2020).

In Chapter 3, we first introduce the simulation of Fukushima & Yajima (2021) in Section 3.2.1. Then we describe the method of our post-process calculations in Section 3.2.2. In Section 3.3 we show the main results of the synthetic observations. We present the velocity distribution of the molecular gas in front of the cluster in Section 3.3.1, and the radial profile of line emissions in Section 3.3.2. Most of the contents in Chapter 3 is to be submitted.

Chapter 4 is devoted to conclusions of the entire thesis.

Chapter 2

Molecular clouds under the FUV feedback

In this chapter, we investigate the properties of the molecular clouds under the FUV feedback by constructing a simple 1D semi-analytic model.

2.1 Model

2.1.1 Methodology

We first describe our model in this section. We consider spherical and uniform density clouds which are characterized by the mass $M_{\rm cl}$ and surface density $\Sigma_{\rm cl}$. The cloud radius $R_{\rm cl}$ and hydrogen number density n_0 are related to $M_{\rm cl}$ and $\Sigma_{\rm cl}$ as

$$R_{\rm cl} = \sqrt{M_{\rm cl}/\pi\Sigma_{\rm cl}} \tag{2.1}$$

$$\begin{aligned} n_0 &= \frac{M_{\rm cl}}{\frac{4}{3}\pi R_{\rm cl}^3 \mu_{\rm H}} \\ &= \frac{3\pi^{1/2}}{4\mu_{\rm H}} M_{\rm cl}^{-1/2} \Sigma_{\rm cl}^{3/2}, \end{aligned} \tag{2.2}$$

where $\mu_{\rm H} = 1.4 m_{\rm H}$ is the mean molecular weight per hydrogen nuclei. We consider clouds with $M_{\rm cl} = 10^4$, 10^5, 10^6 $M_\odot$ below. The surface density is varied so that the resulting number density should fall on a typical range of observed molecular clouds, 30 cm$^{-3} < n_0 <$ 10^4 cm^{-3} (e.g. Tan et al. 2014). Table 2.1 summarizes the ranges of the parameter values we consider.

Our aim is to derive minimum SFE required for cloud disruption $\varepsilon_{\rm min}$ as functions of the cloud mass $M_{\rm cl}$ and surface density $\Sigma_{\rm cl}$.We here focus on the FUV feedback to limit the SFE. For a given set of $(M_{\rm cl}, \Sigma_{\rm cl})$, we start our calculation by putting a star cluster with the mass of $M_* = \varepsilon M_{\rm cl}$ at the origin. Here we first take a trial value for the SFE ε. We envision that an H II region and surrounding photodissociation region (PDR) created by the stellar EUV and FUV radiation expands around the central cluster in the cloud. Following Kim et al. (2016), we calculate the EUV photon number luminosity as

$$S_{\rm EUV} = \Xi_{\rm EUV} M_*, \tag{2.3}$$

Table 2.1: Parameter set

$M_{\rm cl}$ ($M_\odot$)	$\Sigma_{\rm cl}$ ($M_\odot$/pc^2)	$R_{\rm cl}$ (pc)	n_0 (cm^{-3})
10^4	15 – 700	13.2 – 1.94	30 – 10000
10^5	31 – 1506	31.9 – 4.60	30 – 10000
10^6	67 – 3246	68.7 – 9.90	30 – 10000

where the ratio of the stellar mass to the EUV luminosity $\Xi_{\rm EUV}$ is calculated with the SLUG code (Krumholz et al. 2015). Similarly, we calculate the FUV photon number luminosity

$$S_{\rm FUV} = \Xi_{\rm FUV} M_*, \tag{2.4}$$

where we again use the SLUG code to evaluate $\Xi_{\rm FUV}$ (see Section 2.1.2 for details). We assume that Ξ is time-independent. This is a reasonable approximation, since the dynamical timescale $t_{R_{\rm cl}}$ is shorter than the lifetimes of massive main-sequence stars. The dynamics of the expanding H II region and surrounding shell can be described by the analytic formula (see Section 2.1.3). The effects of the FUV radiation on the thermal and chemical structure outside the H II region are then calculated (Section 2.1.4).

These calculations are performed using the arbitrary choice of ε, and we determine the minimum SFE by the following iterative procedure. If ε first assumed is too small, only a small central part of the cloud is affected by the cluster radiation. The further star formation is possible for such a case, meaning that the minimum SFE should be higher. We repeat the calculations with increasing ε incrementally. If ε becomes sufficiently large, the radiative feedback influences the whole natal cloud leaving no room for the further star formation. We assume that the minimum SFE $\varepsilon_{\rm min}$ is determined for such a case (section 2.1.5). The obtained value of $\varepsilon_{\rm min}$ depends on the feedback effects considered. The FUV feedback potentially reduces the SFE in addition to the EUV feedback because it heats the gas outside the H II region to hinder the star formation. The above procedure is basically the same as in Kim et al. (2016), except that we additionally consider the stellar FUV radiation.

2.1.2 Mass-to-luminosity ratio

To calculate the mass-to-luminosity ratio Ξ for the EUV and FUV radiation from a newborn star cluster, we use the SLUG code, a publicly available spectral population synthesis code (Krumholz et al. 2015). We adopt the same settings as in Kim et al. (2016), i.e., with the IMF given by Chabrier (2003), spectral synthesis model Starburst99, and stellar evolution tracks based on the Genova library. We have ran 1000 simulations for each cluster mass bin logarithmically spaced by 0.2 dex in the range of 10^2 $M_\odot \leq M_* \leq 10^5$ $M_\odot$. We assume that the maximum mass of the cluster member star is 100 $M_\odot$. We evaluate the photon number luminosity $S_{\rm EUV}$ and $S_{\rm FUV}$ for the energy ranges of $h\nu > 13.6$ eV (EUV) and 6.0 eV $< h\nu <$ 13.6 eV (FUV), respectively.

Fig. 2.1 presents $\Xi_{\rm EUV}$ (left panel) and $\Xi_{\rm FUV}$ (right panel) as functions of the cluster mass M_*. Each panel shows 10th to 90th percentile range with the blue shade and the median value with the blue circles connected by the solid line. We see that the EUV ratio $\Xi_{\rm EUV}$ rapidly decreases with decreasing the cluster mass; the values for 10^3 $M_\odot$ are more than

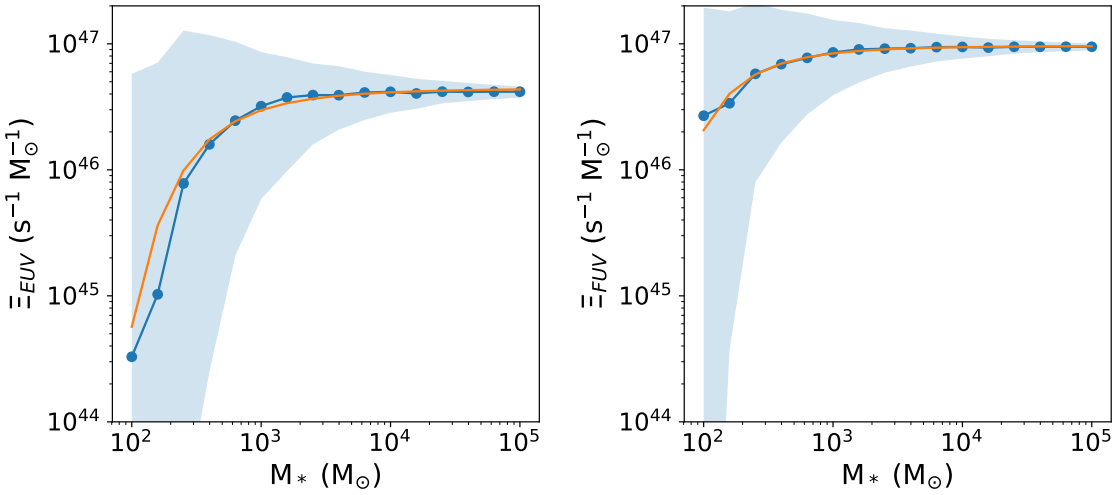

Figure 2.1: The ratio of EUV and FUV photons emitted per unit time to stellar mass $\Xi_{\rm EUV} = S_{\rm EUV}/M_*$ and $\Xi_{\rm FUV} = S_{\rm FUV}/M_*$. The blue line with circles represent the median value, while the shaded area represents the 10th to 90th percentile range from the simulation. Analytical fitting of the median value is showed with the orange line.

one order of magnitude smaller than those for 10^5 M$_\odot$. By contrast, the FUV ratio $\Xi_{\rm FUV}$ only decreases by a factor of a few, at most, from 10^5 M$_\odot$ to 10^3 M$_\odot$. This is because, in comparison to the EUV cases, the less massive stars contribute more to the FUV radiation.

We fit the median value of $\Xi_{\rm EUV}$ and $\Xi_{\rm FUV}$ as the following analytic functions M_*:

$$\log\left(\frac{\Xi_{\rm EUV}}{1{\rm s}^{-1}{\rm M}_\odot^{-1}}\right) = \frac{46.70\chi^6}{2.70+\chi^6}, \tag{2.5}$$

$$\log\left(\frac{\Xi_{\rm FUV}}{1{\rm s}^{-1}{\rm M}_\odot^{-1}}\right) = \frac{47.02\chi^6}{0.92+\chi^6}, \tag{2.6}$$

where $\chi = \log(M_*/{\rm M}_\odot)$. We have used these formulae in our calculations presented in the following part.

2.1.3 Dynamics of expanding H II regions

We here model the dynamical expansion of an H II region created around the cluster in the natal molecular cloud. In what follows we assume that the photoionized gas has the constant temperature $T_{\rm H\,II} = 10^4$ K for simplicity. The initial size of an H II region is determined by the so-called Strömgren radius

$$r_{\rm IF,0} = \left(\frac{3S_{\rm EUV}f_{\rm ion}}{4\pi n_0^2(1-\varepsilon)^2\alpha_{\rm B}}\right)^{1/3}, \tag{2.7}$$

where $\alpha_{\rm B} = 2.59\times10^{-13}(T_{\rm H\,II}/10^4\ {\rm K})^{-0.7}\ {\rm cm^3 s^{-1}}$ is the case B recombination coefficient (Osterbrock 1989), and $f_{\rm ion} = 0.73$ denotes the fraction of the EUV photons absorbed by the gas (not by the dust, Krumholz & Matzner 2009). We note that $f_{\rm ion}$ varies with the product $S_{\rm EUV}n_{\rm H\ II}$ (Draine 2011), although the thermal pressure force and the H II region size only weakly depend on $f_{\rm ion}$ as $r_{\rm IF} \propto f_{\rm ion}^{1/3}$ and $F_{\rm thm} \propto f_{\rm ion}^{1/2}$ (Kim et al. 2016).

Because the internal thermal pressure is much higher than that in the ambient medium, the H II region starts to expand. As considered in Kim et al. (2016), however, the dynamics of the H II region is generally affected by additional effects such as the radiation pressure exerted on the photoionized gas (e.g., Draine 2011) and swept-up shell (e.g., Krumholz & Matzner 2009; Ishiki & Okamoto 2017). However, we omit such additional effects for simplicity. Recent theoretical studies show that the radiation pressure effect is particularly important for disrupting GMCs with high surface densities $\Sigma_{\rm cl} \gtrsim 100\ {\rm M_\odot pc^{-2}}$ (e.g., Murray et al. 2010; Fall et al. 2010). We separately examine its effects on our results in Section 2.3.3.

Once the H II region begins to expand, the ambient gas is swept up to be retained in a shell. The shell is bounded by the ionization front and preceding shock front. The shell mass $M_{\rm sh}$ is estimated as

$$M_{\rm sh} = \frac{4}{3}\pi r_{\rm IF}^3 \rho_0 (1-\varepsilon) - M_{\rm H\,II}. \tag{2.8}$$

Here, $r_{\rm IF}$ is the radial position of the ionization front, $M_{\rm H\,II}$ is the mass of ionized gas,

$$M_{\rm H\,II} \approx \frac{4\pi}{3} r_{\rm IF}^3 \mu_{\rm H} n_{\rm H\,II}, \tag{2.9}$$

where the number density of ionized gas $n_{\rm H\ II}$ varies with ionization front radius as $n_{\rm H\ II} \propto r_{\rm IF}^{-3/2}$. The expansion law, or the time evolution of $r_{\rm IF}$, is derived with the equation of motion of the shell,

$$\frac{d}{dt}(M_{\rm sh} v_{\rm sh}) = F_{\rm out} - F_{\rm in}, \tag{2.10}$$

where $v_{\rm sh} = dr_{\rm sh}/dt$ is the shock velocity, $F_{\rm out}$ and $F_{\rm in}$ represent the forces exerted on the outer and inner surface of the shell. As noted above, we only consider the thermal pressure of the ionized gas as the outward force $F_{\rm out}$,

$$F_{\rm thm} = 4\pi r_{\rm IF}^2 \cdot 2 n_{\rm H\,II} k_{\rm B} T_{\rm H\,II}, \tag{2.11}$$

which scales as $F_{\rm thm} \propto n_{\rm H\ II} r_{\rm IF}^2 \propto r_{\rm IF}^{1/2}$. We ignore $F_{\rm in}$ for simplicity. Equation (2.10) is solved analytically, and we obtain

$$r_{\rm IF}(t) = r_{\rm IF,0}\left(1 + \frac{7}{4}\sqrt{\frac{4}{3}}\frac{c_{\rm s} t}{r_{\rm IF,0}}\right)^{4/7}, \tag{2.12}$$

where $c_{\rm s} = \sqrt{2 k_{\rm B} T_{\rm H\,II}/\mu_{\rm H}}$ is the sound speed in H II region (Hosokawa & Inutsuka 2006). Equation (2.12) differs from the well-known expansion law given by Spitzer (1978) by the factor of $\sqrt{4/3}$, but it actually provides the better approximation as proven by radiation-hydrodynamics numerical simulations (e.g., Bisbas et al. 2015; Kim et al. 2017; Williams et al. 2018). Note that equation (2.12) is basically the same as that given by Kim et al. (2016) but we only consider the thermal pressure of the photoionized gas. Haworth et al. (2015) performed RHD simulations of expanding H II region by taking into account of microphysics such as detailed thermal processes and chemistry. They showed that the expansion is slightly delayed by the order of 10 % at most. It is reasonable to use equation (2.12) in our calculation.

Table 2.2: The thermal and chemical processes included in our model

	Processes	Reference
Heating $\Gamma(n, T, x^*)$	photoelectric heating	1
	ionization by soft X-ray	2
	H_2 photodissociation	3
	H_2 formation	3
Cooling $\Lambda(n, T, x^*)$	fine structure line emission	
	[C II] 158 μm	3
	[O I] 63 μm, 44.2 μm, 145.6 μm	3
	Ly α line emission	4
	CO rotational line emission	5
	collision with dust grains	6
$R^{H^+}_{form}(n, T, x^*)$	ionization by soft X-ray	2
$R^{H^+}_{rec}(n, T, x^*)$	case B recombination	7
$R^{H_2}_{form}(n, T, x^*)$	dust catalysis	8
	associative detachment	3
$R^{H_2}_{dis}(n, T, x^*)$	photodissociation	8,9
	dust collision	8
$R^{CO}_{form}(n, T, x^*)$	CO formation	10, 11
$R^{CO}_{dis}(n, T, x^*)$	photodissociation	10, 11

References: (1) Bakes & Tielens (1994); (2) Wolfire et al. (1995); (3) Hollenbach & McKee (1979); (4) Spitzer (1978); (5) McKee et al. (1982); (6) Hollenbach & McKee (1989); (7) Osterbrock (1989); (8) Tielens & Hollenbach (1985); (9) Draine & Bertoldi (1996); (10) Langer (1976); (11) Nelson & Langer (1997)

2.1.4 Thermal and chemical structure of photodissociation regions

For every snapshot of an expanding H II region within the cloud, we calculate the thermal and chemical structure in the surrounding photodissociation region (PDR). Below we consider the following seven chemical species of e^-, H^+, H^0, H_2, C^+, O^0 and CO. We assume the total abundance of C and O atoms as $x_C = 3.0 \times 10^{-4}$ and $x_O = 4.6 \times 10^{-4}$ (Wolfire et al. 1995), where x denotes the number fraction relative to the hydrogen nuclei.

One-zone thermal and chemical equilibrium model

We make use of the one-zone modeling of the thermal and chemical equilibrium state of the interstellar medium (e.g., Wolfire et al. 1995; Koyama & Inutsuka 2000). Consider the gas with a given density n exposed by a FUV radiation field with G_0. We determine the unknown variables, the gas temperature T and chemical number fractions x_{H^+}, x_{H_2}, x_{CO}, by

solving the following equations

$$\frac{de}{dt} = \Gamma(n, T, x^*) - \Lambda(n, T, x^*) \tag{2.13}$$

$$\frac{dx_{\rm H^+}}{dt} = R^{\rm form}_{\rm H^+}(n, T, x^*) - R^{\rm rec}_{\rm H^+}(n, T, x^*) \tag{2.14}$$

$$\frac{dx_{\rm H_2}}{dt} = R^{\rm form}_{\rm H_2}(n, T, x^*) - R^{\rm dis}_{\rm H_2}(n, T, x^*) \tag{2.15}$$

$$\frac{dx_{\rm CO}}{dt} = R^{\rm form}_{\rm CO}(n, T, x^*) - R^{\rm dis}_{\rm CO}(n, T, x^*) \tag{2.16}$$

where e is internal energy of the gas, Γ and Λ are the heating and cooling rates, and x^* represents $(x_{\rm H^+}, x_{\rm H_2}, x_{\rm CO})$. In the present study, we only consider $\rm C^+$ and CO as carbon compounds and thus set $x_{\rm C^+} = x_{\rm C} - x_{\rm CO}$.

A full list of thermal and chemical processes associated with the terms on the R.H.S of equations (2.13) - (2.16) is presented in Table 2.2. We here only briefly describe some of them. Those readers who are interested in more details may refere to the references therein. As the heating processes, we incorporate the photoelectric emission from grains and $\rm H_2$ dissociation by the FUV radiation, ionization by the background soft X-ray radiation, and $\rm H_2$ formation releasing the binding energy. The radiative cooling is primarily caused via the line emission of [C II], [O I], Ly-α, and CO. We assume the optically-thin limit for these line emission. It is equivalent to ignoring the trapping effect, for which possible effects on our conclusions are discussed in Section 2.3.2. To avoid overcooling, we set the minimum gas temperature to be 8 K. Regarding the formation of CO molecules, we adopt the simple method given by Nelson & Langer (1997), where CO molecules are approximately formed from $\rm C^+$ ions and O atoms. Gong et al. (2018) pointed out that the Nelson & Langer (1999) chemical network significantly underestimates CO abundance for $n \lesssim 500$ cm^{-3} and $A_{\rm V}$ ¡ 5. However, we use the chemical network by Nelson & Langer in the present study, since we focus on the CO abundance at dense shell where $n > 10^4$ cm^{-3}. We also assume the constant dust temperature $T_{\rm d} = 8$ K for the all cases considered. The dust temperature is used to estimate the reformation rate of $\rm H_2$ molecules and the thermal gas-dust coupling rate via collisions. We also investigate the effects of varying $T_{\rm d}$ in our calculations in Section 2.3.2.

Time-evolution of multi-zone structure

We calculate the spatial variation of the thermal and chemical state in the PDR around an H II region by repeating the one-zone calculations as follows. At a given time $t = t_j$, the radius and mass of the shell, $M_{\rm sh}(t_j)$ and $r_{\rm sh}(t_j)$, are described by equations (2.8) and (2.12). By setting radial grids, we discretize the outer PDR including the shell into cells with the column density $\Delta N_{\rm H} \sim 10^{19}$ cm^{-2} per each which corresponds to $A_V = 5.0 \times 10^{-3}$ with the conversion law of $A_V = 5.0 \times 10^{-22} N_{\rm H}$. The number of the grids is typically ~ 1000. The distance from the ionization front to the i-th grid r_i is

$$r_i = r_{\rm IF}(t_j) + \sum_{k=0}^{i} \Delta N_{\rm H}/n_k, \tag{2.17}$$

which corresponds to the dust optical depth in the outward direction

$$\tau_{\mathrm{in},\,i} = \sigma_d \sum_{k=0}^{i} \Delta N_{\mathrm{H}}, \tag{2.18}$$

and the dust optical depth from the edge of the cloud $\tau_{\mathrm{out},\,i}$

$$\tau_{\mathrm{out},\,i} = \sigma_d \sum_{k=i}^{N} \Delta N_{\mathrm{H}}, \tag{2.19}$$

The normalized FUV flux at $r = r_i$ is written as

$$G_i = \frac{1}{F_{\mathrm{H}}} \frac{S_{\mathrm{FUV}}}{4\pi r_i^2} \exp(-\tau_{\mathrm{in}},\, i) + G_{\mathrm{bg}} \exp(-\tau_{\mathrm{out},\,i}), \tag{2.20}$$

where N is the total number of the grids, $\sigma_{\mathrm{d}} = 10^{-21}$ cm^{2}H^{-1} is the absorption cross section by dust grains per hydrogen nucleus, and $F_{\mathrm{H}} = 1.21 \times 10^7$ cm^{-2}s^{-1} is the normalization factor which represents the background field near the Solar system (the so-called Habing unit, i.e., Habing 1968; Draine & Bertoldi 1996) . The last term of the unity in equation (2.20) represents this background exactly. The mass summation over the cells located at $r \leq r_i$ is

$$M_i = \sum_{k=0}^{i} 4\pi r_k^2 \mu_{\mathrm{H}} \Delta N_{\mathrm{H}}. \tag{2.21}$$

By comparing M_i to the total shell mass M_{sh}, we judge whether the i-th cell is still within the shell or not. As far as $M_i < M_{\mathrm{sh}}$, the cell is regarded as a part of the shell. We determine the thermal and chemical states of such cells in an iterative manner as follows. We assume that the gas pressure within the shell is equal to that of the H II region, $P_{\mathrm{th}} = 2n_{\mathrm{HII}} k_{\mathrm{B}} T_{\mathrm{HII}}$. So we initially provide the pressure instead of the density in a one-zone calculation, unlike in Section 2.1.4. With the given pressure P_{th} and FUV field G_i, we calculate the unknown variable (T_i, x_i^*) by solving equations (2.13)-(2.16) so that the resulting pressure $P_{\mathrm{sh}} = n_i(1 + x_{e^-} - x_{\mathrm{H}_2}/2) k_{\mathrm{B}} T_i$ matches P_{th}. By doing that, we also determine the number density n_i as well as (T_i, x_i^*). Once (n_i, T_i, x_i^*) are fixed, we then move on to the next $(i+1)$-th cell and repeat the same procedures. If M_i exceeds M_{sh}, the following cells are considered to be outside of the shell as the un-shocked ambient gas. We take exactly the same method as in Section 2.1.4 for such cells; we calculate (T_i, x_i^*) for the given number density $n_0(1-\varepsilon)$ and FUV field G_i. We continue the calculations until reaching the cloud edge, i.e., for $M_i < M_{\mathrm{gas}} = M_{\mathrm{cl}}(1-\varepsilon) - M_{\mathrm{H\,II}}$.

2.1.5 Cloud disruption criteria

To determine the minimum SFE of the cloud, we need some criteria of the cloud disruption as in Kim et al. (2016). We investigate the effects of the FUV feedback on top of the EUV feedback previously studied. So we first use the exactly the same criterion as in Kim et al. (2016):

Criterion 1 (EUV feedback): An H II region and shell are assumed to expand as far as the shell velocity $v_{\rm sh}$ is larger than the critical velocity $v_{\rm bind} = \sqrt{GM_{\rm cl}(1+\varepsilon)/R_{\rm cl}}$,

$$v_{\rm bind} \simeq 5 \text{ km/s} \left(\frac{M_{\rm cl}}{10^5 \text{ M}_\odot}\right)^{1/4} \left(\frac{\Sigma_{\rm cl}}{10^2 \text{ M}_\odot\text{pc}^{-2}}\right)^{1/4} (1+\varepsilon)^{1/2}. \tag{2.22}$$

If the trial value of ε is too small, the expansion stalls well before the shell reaches the cloud edge. We iteratively increase ε until $v_{\rm sh} = v_{\rm bind}$ is satisfied at the cloud edge, i.e., $r = R_{\rm cl}$. This gives the minimum SFE.

Note that the above is not the only criterion investigated in Kim et al. (2016). They have also adopted other criteria, showing that the obtained minimum SFE does not largely change. Since our aim is to study the effects of the FUV radiation, we only focus on one representative case.

Criterion 2 (FUV feedback): We assume that the star formation is suppressed in a warm PDR, where the gas temperature is above the threshold value 100 K. Technically, if the trial value of ε is too small, the temperature outside of the shell is at least partly lower than 100 K. We iteratively increase ε until the gas is heated above 100 K everywhere outside the shell at a certain epoch. This gives the minimum SFE.

Although the temperature is raised to $\sim 100 - 1000$ K in the PDR, the corresponding sound speed is much smaller than that of the photoionized gas. Therefore, as often presumed, the resulting FUV feedback should be weaker than the EUV feedback. The FUV effects would not operate to disrupt the entire structure of the molecular clouds. We rather suppose that the star formation in the PDR is locally hindered with the lack of the cold (~ 10 K) materials. Since the exact strength of the FUV feedback is uncertain, we also consider Criterion 1 for limiting the SFEs. We only estimate effects of the FUV feedback on the chemical compositions of cloud remnants for such cases.

2.2 Results

2.2.1 Time evolution of thermal and chemical structure

First we present typical evolution of the thermal and chemical structure in the PDR around an H II region. Here we spotlight one particular case with the molecular cloud mass $M_{\rm cl} = 10^4$ M$_\odot$ and surface density $\Sigma_{\rm cl} = 300$ M$_\odot$pc^{-2}. We follow the evolution with a star cluster with $M_* = \varepsilon_{\rm min} M_{\rm cl} \simeq 1220$ M$_\odot$ formed at the cloud center[1]. The corresponding stellar EUV and FUV photon number luminosities are $S_{\rm EUV} \simeq 4.2\times10^{49}$ sec^{-1} and $S_{\rm FUV} \simeq 8.0\times10^{49}$ sec^{-1} respectively.

Fig. 2.2 shows the position of ionization front $r_{\rm IF}$ (equation 2.12) and shell $r_{\rm sh} = r_{\rm IF} + \sum \Delta N_{\rm H}/n_i$ as a function of time. Fig. 2.3 shows the time evolution of the one-dimensional thermal and chemical structure at (a) $t = 0$, (b) $t = 0.5\,t_{R_{\rm cl}}$, and (c) $t = t_{R_{\rm cl}}$, where $t_{R_{\rm cl}}$ is

[1] For this representive case, we find that the minimum SFE $\varepsilon \simeq 0.12$ is insensitive to the choice of cloud disruption criteria (see also Section 2.2.2).

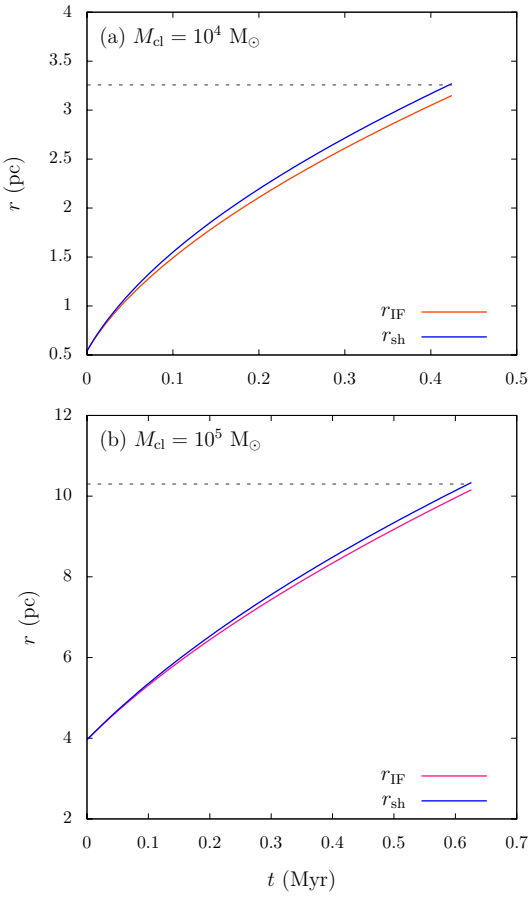

Figure 2.2: The positions of the ionization front $r_{\rm IF}$ (red solid line) and the shock front $r_{\rm sh}$ (blue solid line) as functions of time for the cases with (a) $M_{\rm cl} = 10^4$ M$_\odot$ ($\Sigma_{\rm cl} = 300$ M$_\odot$pc^{-2}) and with (b) $M_{\rm cl} = 10^5$ M$_\odot$ ($\Sigma_{\rm cl} = 300$ M$_\odot$pc^{-2}) in the upper and lower panels, respectively. The black dashed line in each panel indicates the position of the outer edge of the cloud; (a) $R_{\rm cl} = 3.25$ pc and (b) $R_{\rm cl} = 10.3$ pc.

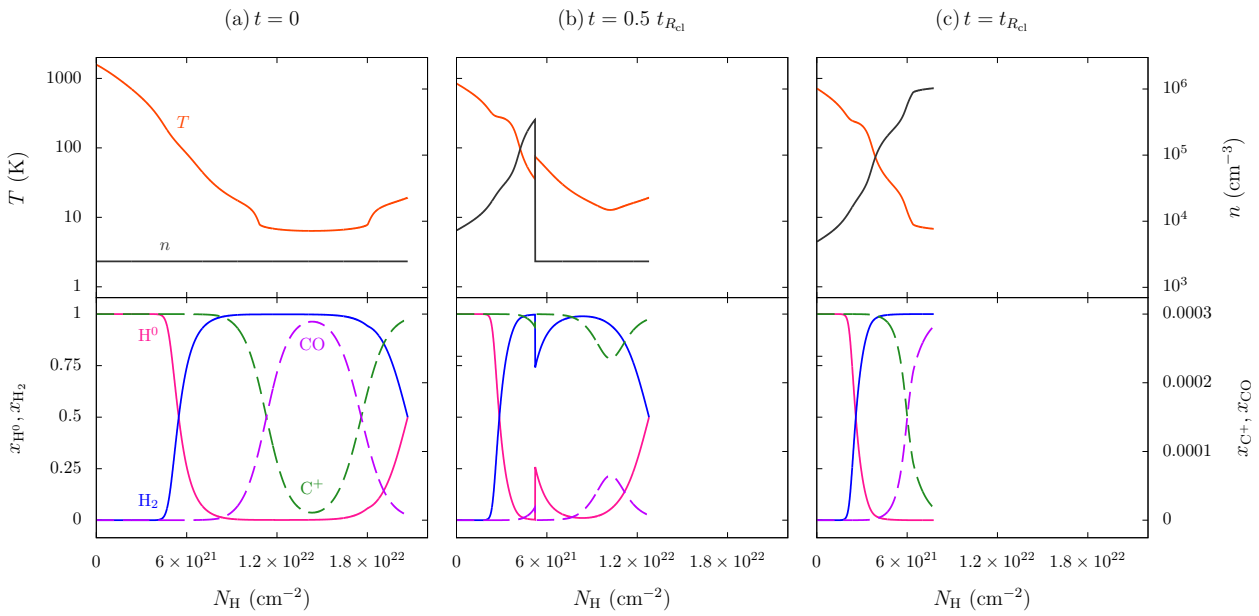

Figure 2.3: Time evolution of the thermal and chemical structure in the photodissociation region around an H II region. The cloud mass and surface density are $M_{\rm cl} = 10^4$ M$_\odot$ and $\Sigma_{\rm cl} = 300$ M$_\odot$pc^{-2} for this case. The panels (a), (b), and (c) show the snapshots at the different epochs of (a) $t = 0$, (b) $t = 0.5\,t_{R_{\rm cl}}$ and (c) $t = t_{R_{\rm cl}}$, where $t_{R_{\rm cl}}$ is the time when the shell reaches the cloud edge. The horizontal axis denotes the column density of hydrogen nuclei measured from the ionization front; that is, $N_{\rm H} = 0$ corresponds to $r_{\rm IF}$ and the maximum value of $N_{\rm H}$ corresponds to $R_{\rm cl}$. *Top:* Plotted are the gas temperature (red line) and density (gray line), for which the scaling is presented with the left- and right-hand axis. *Bottom:* Plotted are the fractional abundances of H I (red solid line), H_2 (blue solid line), C II (green dashed line), and CO (purple dashed line). The left-hand (right-hand) axis is used for scaling of H I and H_2 (C II and CO) abundances.

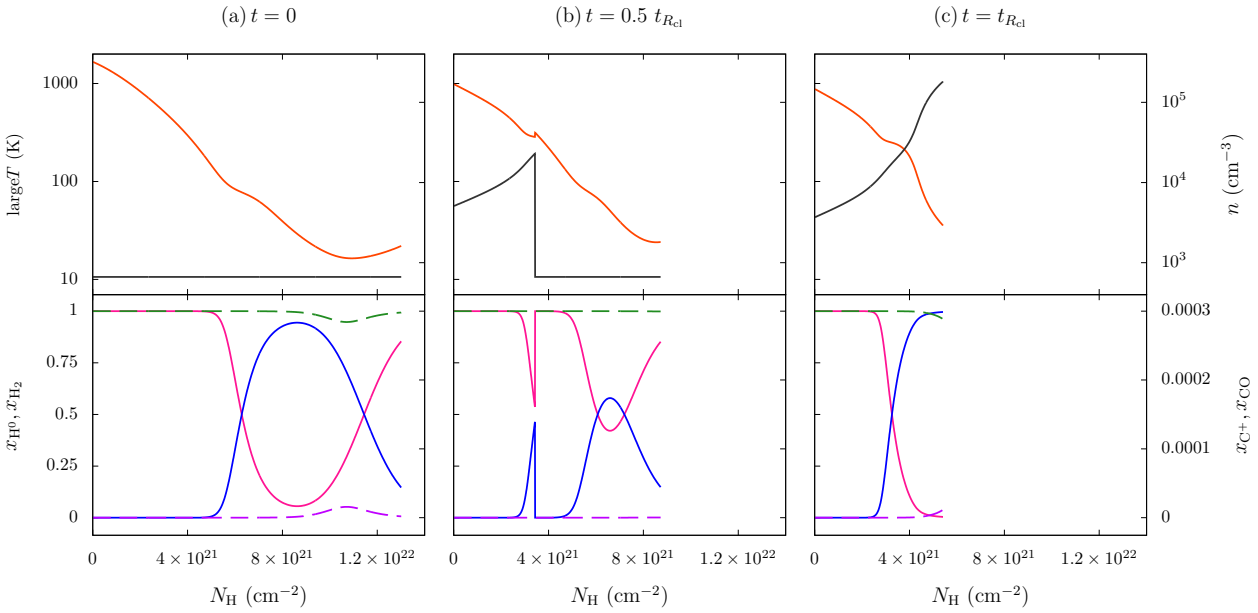

Figure 2.4: Same as Fig. 2.3, except for the higher cloud mass of $M_{\rm cl} = 10^5\ {\rm M}_\odot$ and surface density $\Sigma_{\rm cl} = 300\ {\rm M}_\odot{\rm pc}^{-2}$.

the time when the shell reaches the cloud edge. Note that the total column density deceases with time in this figure. This is explained by the difference of the geometry: the initial and final column density $N_0 = n_0 R_{\rm cl}$ and $N_{\rm H}^{\rm shell}$ are related as

$$M_{\rm gas} = \frac{4}{3}\pi R_{\rm cl}^2 N_0 \mu_{\rm H} \sim 4\pi R_{\rm cl}^2 N_{\rm H}^{\rm shell} \mu_{\rm H}, \tag{2.23}$$

where we approximate $r_{\rm IF}(t_{R_{\rm cl}})$ as $R_{\rm cl}$. Then we find $N_{\rm H}^{\rm shell} \sim N_0/3$.

Fig. 2.3 (a) presents the snapshot at $t = 0$, when the initial Strömgren sphere is created. Since at this epoch the shell has not appeared yet, the density is constant everywhere. The temperature rapidly grows toward the central cluster because of the efficient photoelectric heating by the strong stellar FUV radiation. In the outer part with $1.2 \times 10^{22}\ {\rm cm}^{-2} \lesssim N_{\rm H} \lesssim 1.8 \times 10^{22}\ {\rm cm}^{-2}$, however, the temperature profile is flat since we set the minimum gas temperature at 8 K (see Section 2.1.4). In the lower panel, we see that the hydrogen molecules are dissociated by the cluster FUV radiation for $N_{\rm H} \lesssim 4.0 \times 10^{21}\ {\rm cm}^{-2}$.

Fig. 2.3 (b) shows that the swept-up shell has emerged by the epoch of $t = 0.5\, t_{R_{\rm cl}}$ and $r_{\rm IF} = 2.2$ pc. The discontinuity of physical quantities at $N_{\rm H} \simeq 5.4 \times 10^{21}\ {\rm cm}^{-2}$, which corresponds to the preceding shock front, or the shell outer edge represented by $r_{\rm sh}$. Within the shell, the temperature decreases outward as the FUV flux drops owing to the dust attenuation. The density inversely increases, because the thermal pressure is assumed to be fixed at the value of the H II region. The hydrogen dissociation front is shifted to the lower column density at $N_{\rm H} \simeq 2.5 \times 10^{21}\ {\rm cm}^{-2}$ than in panel (a) because of the efficient self-shielding of H_2 molecules within the dense shell. By contrast, there is only little amount of CO molecules within the shell. The temperature just outside the shell is slightly higher than that inside the shell because the [C II] line emission, which is the dominant coolant of the cloud, is less efficient with the lower density (see also Section 2.2.2). Since the density

differs by approximately 2 orders of magnitude across the shock front, the cooling efficiency also differs.

Fig. 2.3 (c) shows the final snapshot for the current case, when all of the cloud materials are swept into the shell. Unlike the previous snapshot, the CO dissociation front is taken into the shell at $N_{\rm H} \simeq 6.0 \times 10^{21}$ cm^{-2} because the shell column density has become so large that CO molecules are protected against the cluster FUV radiation with the dust attenuation. As shown below, this is the final snapshot when the minimum SFE is determined, and the swept-up gas on the shell is, so to speak, the remnant of the molecular cloud. It is evident that the chemical composition of such a cloud remnant is not homogeneous. There are some amount of H_2 molecules, but only a small part of those is associated with CO molecules. We return to this point later in Section 2.2.3.

Next we show the case where CO molecules are almost completely destroyed by FUV radiation. Fig. 2.4 represents the case with $M_{\rm cl} = 10^5$ M$_\odot$ and $\Sigma_{\rm cl} = 300$ M$_\odot$pc^{-2}. The central cluster mass is 2.6×10^4 M$_\odot$ and corresponding stellar EUV and FUV photon number luminosity is $S_{\rm EUV} \simeq 1.2 \times 10^{51}$ s^{-1} and $S_{\rm FUV} \simeq 2.5 \times 10^{51}$ s^{-1}, respectively. The clear difference from the case with $M_{\rm cl} = 10^4$ M$_\odot$ is that CO molecules do not survive throughout the time evolution. This behavior is mainly explained by the difference of G_0 (see Section 2.2.3 for detailed discussion).

2.2.2 Star formation efficiency of molecular clouds

Limiting star formation efficiency by FUV radiation

In this section we investigate the SFE of the molecular clouds set by the EUV and FUV feedback effects. Consider an expanding H II region and surrounding PDR around a newly-born cluster in a given molecular cloud. If the cluster is not sufficiently massive (or luminous), only a small part of the cloud near the cluster would be affected by the feedback; further star formation would occur in the remnant part until enough stars have formed to halt further star formation and destroy the whole cloud. Hence there should be the minimum value of the SFE $\varepsilon_{\rm min}$ above which the cloud is destroyed by radiative feedback. We calculate $\varepsilon_{\rm min}$ as functions of $M_{\rm cl}$ and $\Sigma_{\rm cl}$ in the iterative manner as outlined in Section 2.1.1.

Each panel in Fig. 2.5 shows the minimum SFE obtained as a function of the cloud surface density $\Sigma_{\rm cl}$ for the same mass $M_{\rm cl}$. The cloud masses of $M_{\rm cl} = 10^4$, 10^5 and 10^6 M$_\odot$ are assumed for panels (a), (b) and (c), respectively.

The gray line in each panel represents the case where only the EUV feedback is considered (Criterion 1, $\varepsilon_{\rm min,1}$). We see that $\varepsilon_{\rm min,1}$ is an increasing function of $\Sigma_{\rm cl}$, as shown in Kim et al. (2016). Such a behavior is well understood by considering the $\Sigma_{\rm cl}$-dependences of the cloud radius $R_{\rm cl}$ and initial Strömgren radius $r_{\rm St,0}$: $R_{\rm cl} \propto \Sigma_{\rm cl}^{-1/2}$ and $r_{\rm St,0} \propto \Sigma_{\rm cl}^{-1}$ for a given $M_{\rm cl}$ and $S_{\rm EUV}$. It means that, with increasing $\Sigma_{\rm cl}$, the typical size of the H II region $r_{\rm St,0}$ relative to the cloud size $R_{\rm cl}$ decreases. The more massive or luminous cluster is necessary for the H II region to cover the whole cloud for such a case. Thus the resulting $\varepsilon_{\rm min}$ is higher for higher surface density. Kim et al. (2016) provide the analytic formula describing this dependence as

$$\frac{\varepsilon_{\rm min}}{(1-\varepsilon_{\rm min}^2)^2} = \left(\frac{\pi^{5/4} G}{\eta_{\rm th} \mathcal{T}}\right)^2 M_{\rm cl}^{1/2} \Sigma_{\rm cl}^{5/2}, \tag{2.24}$$

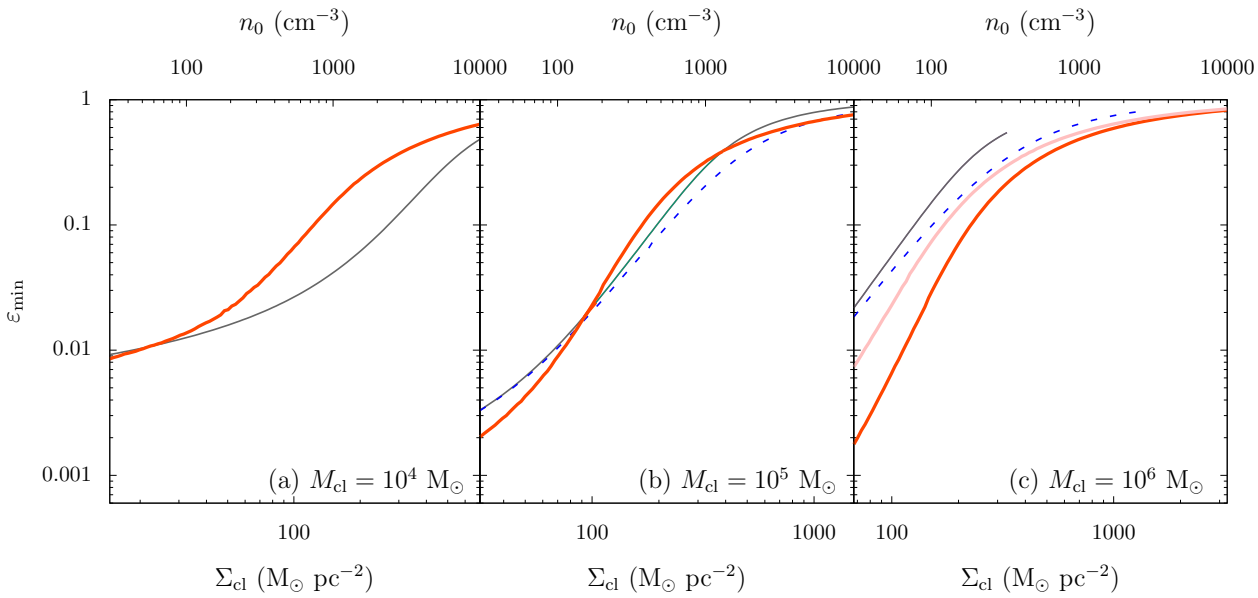

Figure 2.5: The minimum star formation efficiency (SFE) $\varepsilon_{\rm min}$ calculated as functions of the cloud surface density $\Sigma_{\rm cl}$. The different cloud masses of $M_{\rm cl} = 10^4$ M$_\odot$, $M_{\rm cl} = 10^5$ M$_\odot$ and $M_{\rm cl} = 10^6$ M$_\odot$ are assumed for panels (a), (b) and (c). In each panel, the thick red line represents the case where the SFE is limited by both the EUV and FUV feedback (Criterion 2). The black line represents the reference case only with the EUV feedback (Criterion 1), as considered in Kim et al. (2016). The blue dashed lines in panel (b) and (c) represents the cases where effects of the radiation pressure is included for the dynamics of the H II region expansion. In panel (c), the red shaded zone represents the range where the threshold temperature is varied between 50 K and 300 K in Criterion 2, and the purple dot-dashed line represents the case with lower C and O abundances, $x_{\rm C} = 1.4 \times 10^{-4}$ (Cardelli et al. 1996) and $x_{\rm O} = 2.8 \times 10^{-4}$ (Cartledge et al. 2004). Note that each panel shows a different range of $\Sigma_{\rm cl}$.

where $\eta_{\rm th} = 9/4$ and $\mathcal{T} = 8\pi k_{\rm B} T_{\rm H\,II}[3 f_{\rm ion}\Xi_{\rm EUV}/4\pi\alpha_{\rm B}]^{1/2}$. Note that the gray line in each panel representing the EUV feedback is not identical because of the dependence of $\varepsilon_{\rm min} \propto M_{\rm cl}^{1/2}$ in equation (2.24).

In our model, the gas density is proportional to $(1-\varepsilon)$ and the photon number flux $S_{\rm EUV}$ is proportional to ε, so that the size of the initial H II region becomes increasingly larger for higher ε. Thus there is a critical ε over which $r_{\rm IF,0} \geq R_{\rm cl}$. This occurs when the cloud surface density and mass are both large (see also Kim et al. 2016). This explains why the gray solid line stops in the middle of the diagram in panel (c).

Let us next examine the effect of the FUV radiation on limiting the minimum SFE. The red line in each panel of Fig. 2.5 represents the cases with FUV feedback (i.e., Criterion 2, $\varepsilon_{\rm min,2}$). Comparing the red line to the gray line, we can evaluate the effect of the FUV feedback on top of the EUV feedback. The minimum SFE is defined as $\varepsilon_{\rm min} = \min(\varepsilon_{\rm min,1}, \varepsilon_{\rm min,2})$.

Fig. 2.5 (a) shows that introduction of the FUV feedback does not change the SFEs in the cases with cloud mss $M_{\rm cl} = 10^4$ M$_\odot$; $\varepsilon_{\rm min} = \varepsilon_{\rm min,1}$. For more massive clouds with $M_{\rm cl} = 10^6$ M$_\odot$ (panel c), by contrast, the FUV feedback is quite important; $\varepsilon_{\rm min} = \varepsilon_{\rm min,2}$. For a given $\Sigma_{\rm cl}$, the minimum SFE is reduced by the inclusion of the FUV feedback by one order of magnitude, at maximum. In particular, the difference is larger at smaller surface density, $\Sigma_{\rm cl}$. In the case with intermediate mass of $M_{\rm cl} = 10^5$ M$_\odot$ (panel b), the resulting $\varepsilon_{\rm min}$ is only slightly (by about 10 %) reduced by the FUV feedback effect at the lower and higher ends of $\Sigma_{\rm cl}$, i.e., $\Sigma_{\rm cl} \lesssim 100$ M$_\odot$pc^{-2} and $\Sigma_{\rm cl} \gtrsim 400$ M$_\odot$pc^{-2}.

We also study the parameter dependencies of SFEs in the case with cloud mass $M_{\rm cl} = 10^6$ M$_\odot$, where the effect of the FUV feedback is the most remarkable. We consider the different threshold temperatures between 50 K and 300 K, and lower abundances of carbon and oxygen (e.g., Cardelli et al. 1996; Cartledge et al. 2004). We find that the variations of SFEs are the most visible when the surface density is low, and the differences amount to a factor of ten at most. However, the overall trend remains the same irrespective of parameter values.

To summarize, the FUV feedback is sufficiently effective in massive and low surface density clouds. We further analyze our calculations to interpret the results in next Section 2.2.2.

Interpreting Results

As shown in Section 2.2.2, the impacts of the FUV feedback on limiting the minimum SFE depends on the cloud parameters such as the cloud mass $M_{\rm cl}$ and surface density $\Sigma_{\rm cl}$. Here we further look into our results to consider what causes such variations.

First we investigate the case of clouds with $M_{\rm cl} = 10^5$ M$_\odot$. Since the heating in PDRs is assumed to limit the SFEs, we consider the temperature just outside of the shell, $T_{\rm out}$. The thick black line in Fig. 2.6(a) shows $T_{\rm out}$ as a function of $\Sigma_{\rm cl}$ at the cloud edge $r = R_{\rm cl}$ at $t = t_{R_{\rm cl}}$, i.e., when the SFE is determined by the EUV feedback only (Criterion 1). We see that $T_{\rm out}$ has the local minimum at $\Sigma_{\rm cl} \simeq 200$ M$_\odot$pc^{-2}. Since the PDR is primarily heated up via the photoelectric emission from grains, the local FUV flux $G_{\rm out}$ is a key quantity to determine $T_{\rm out}$. According to equations (2.1) and (2.20), $G_{\rm out}$ is proportional to $S_{\rm FUV}\Sigma_{\rm cl}/M_{\rm cl} \propto \varepsilon_{\rm min}\Sigma_{\rm cl}$ (neglecting dust attenuation). It follows that $G_{\rm out}$ monotonically increases with increasing $\Sigma_{\rm cl}$, because the minimum SFE or $S_{\rm FUV}$ increases with $\Sigma_{\rm cl}$ (Fig. 2.5a). With the above facts,

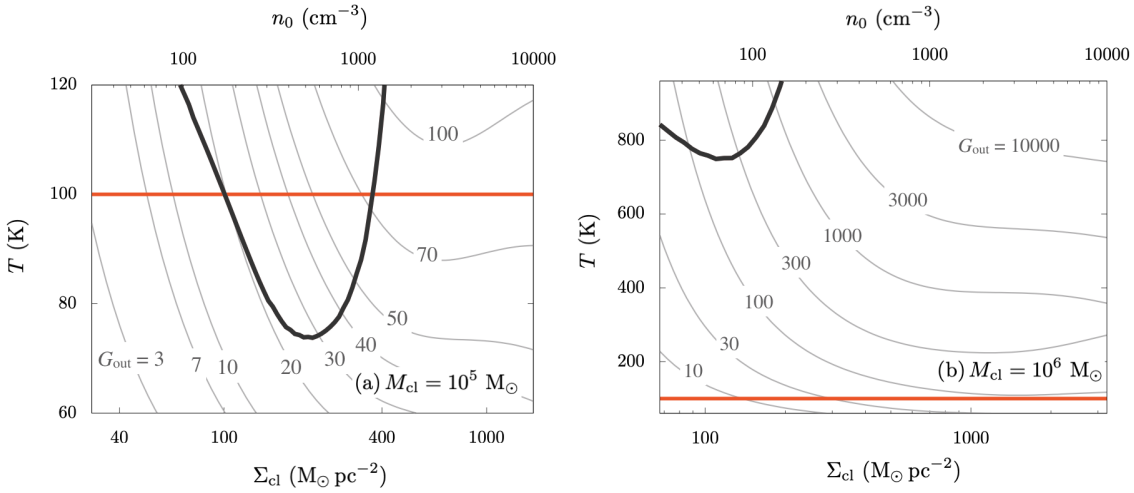

Figure 2.6: Effects of the FUV heating in limiting the minimum SFE with $M_{\rm cl} = 10^5$ M$_\odot$ (panel a) and $M_{\rm cl} = 10^6$ M$_\odot$ (b). In each panel, the thick black line represents the gas temperature at the cloud outer edge when the minimum SFE is determined only by the EUV feedback (Criterion 1, the gray lines in Fig. 2.5). In such a case, an expanding H II region and surrounding shell just fill the whole cloud, and the "cloud edge" corresponds to the un-shocked gas just outside the shell. The red line represents the critical temperature 100 K, above which the star formation is assumed to be suppressed by the FUV feedback (Criterion 2). At $\Sigma_{\rm cl}$ for which the red curve exceeds the red line, the gas is heated up above 100 K before the shell reaches the cloud edge, meaning that the SFE should be primarily limited by the FUV feedback if included. The gray contours denote the equilibrium temperature for different values of FUV flux $G_{\rm out}$ as functions of the density. We note that, in panel (b), the vertical axis covers the much larger range of the temperature than in panel (a).

one may ask why $T_{\rm out}$ decreases with $\Sigma_{\rm cl}$ for $\Sigma_{\rm cl} \lesssim 200$ $\mathrm{M_\odot pc^{-2}}$, where $G_{\rm out}$ *increases* with $\Sigma_{\rm cl}$. This is explained by the nature of the [C II] line cooling, which dominates over other processes. The [C II] cooling rapidly becomes efficient with the increasing density n (or $\Sigma_{\rm cl}$) for $n \ll n_{\rm cr} \simeq 2000$ $\mathrm{cm^{-3}}$. Such a trend is illustrated as gray lines in Fig. 2.6, which show the equilibrium gas temperature as a function of density at for different values of $G_{\rm out}$ clearly show such a trend. Since the slope of the contour lines are so steep that $T_{\rm out}$ drops while $G_{\rm out}$ increases with $\Sigma_{\rm cl}$.

Let us compare $T_{\rm out}$ with the threshold temperature for the FUV feedback, 100 K. We see that $T_{\rm out}$ exceeds 100 K in both the lower and higher sides of $\Sigma_{\rm cl}$. It suggests that the dertruction by the FUV feedback is more effective than dynamical disruption. Since the temperature gets lower with the lower $G_{\rm out}$ at a given $\Sigma_{\rm cl}$, only the smaller $S_{\rm FUV}$ (or smaller ε) is enough to realize $T_{\rm out} = 100$ K. The above explains why ε is reduced by the FUV feedback in the higher and lower sides of $\Sigma_{\rm cl}$ in Fig. 2.5.

Fig. 2.6(b) shows the same plots as Fig. 2.6(a) but for the cases with more massive clouds with $M_{\rm cl} = 10^6$ $\mathrm{M_\odot}$, where the FUV feedback effects are more remarkable than other cases. In this case, $T_{\rm out}$ is much higher than the threshold temperature 100 K for any range of $\Sigma_{\rm cl}$. This is due to the dependence of $G_{\rm out} \propto S_{\rm FUV}\Sigma_{\rm cl}/M_{\rm cl}$ again. With a fixed value of $\Sigma_{\rm cl}$, $G_{\rm out}$ is larger with the higher $M_{\rm cl}$ because $G_{\rm out} \propto \varepsilon S_{\rm FUV}/M_* = \varepsilon \Xi_{\rm FUV}$ and ε is enhanced following equation (2.24). The SFEs required to disrupt the natal cloud is much smaller than the case only with the EUV feedback. Fig. 2.6(b) also suggests that even with somewhat large threshold temperature $\lesssim 700$ K the FUV feedback should still reduce the minimum SFE $\varepsilon_{\rm min}$.

2.2.3 Chemical compositions of molecular cloud remnants

Our calculations suggest that the EUV and FUV radiative feedback from forming clusters jointly contribute to reduce the SFE of molecular clouds. In this section, we cast light on the gas that has not been used for the star formation, i.e., the "remnants" of the clouds. The cloud remnants still retain a large part of the cloud materials because the obtained SFEs are much smaller than the unity for many cases. We here focus on the chemical compositions of the cloud remnants, which are also followed in our calculations.

We calculate the masses of H I, CO-dark and CO-bright H_2 gases as follows:

$$M_{\rm H\ I} = \sum_{k=0}^{N} 4\pi r_k^2 \mu_{\rm H} \Delta N_{\rm H} x_{\rm H^0}, \tag{2.25}$$

$$M_{\rm H_2\,w/o\,CO} = \sum_{k=0}^{N} 4\pi r_k^2 \mu_{\rm H} \Delta N_{\rm H} x_{\rm H_2} x_{\rm C^+}/x_{\rm C}, \tag{2.26}$$

$$M_{\rm H_2\,w/\,CO} = \sum_{k=0}^{N} 4\pi r_k^2 \mu_{\rm H} \Delta N_{\rm H} x_{\rm H_2} x_{\rm CO}/x_{\rm C}. \tag{2.27}$$

First we consider the cases with the fixed cloud mass $M_{\rm cl} = 10^5$ $\mathrm{M_\odot}$. Fig. 2.7 (a) presents the mass fraction of the gas with the different chemical properties as functions of $\Sigma_{\rm cl}$. The neutral and molecular hydrogens are the dominant components of the cloud remnants, and they occupy 70 % and 30 % of the total mass respectively. In particular, we distinguish

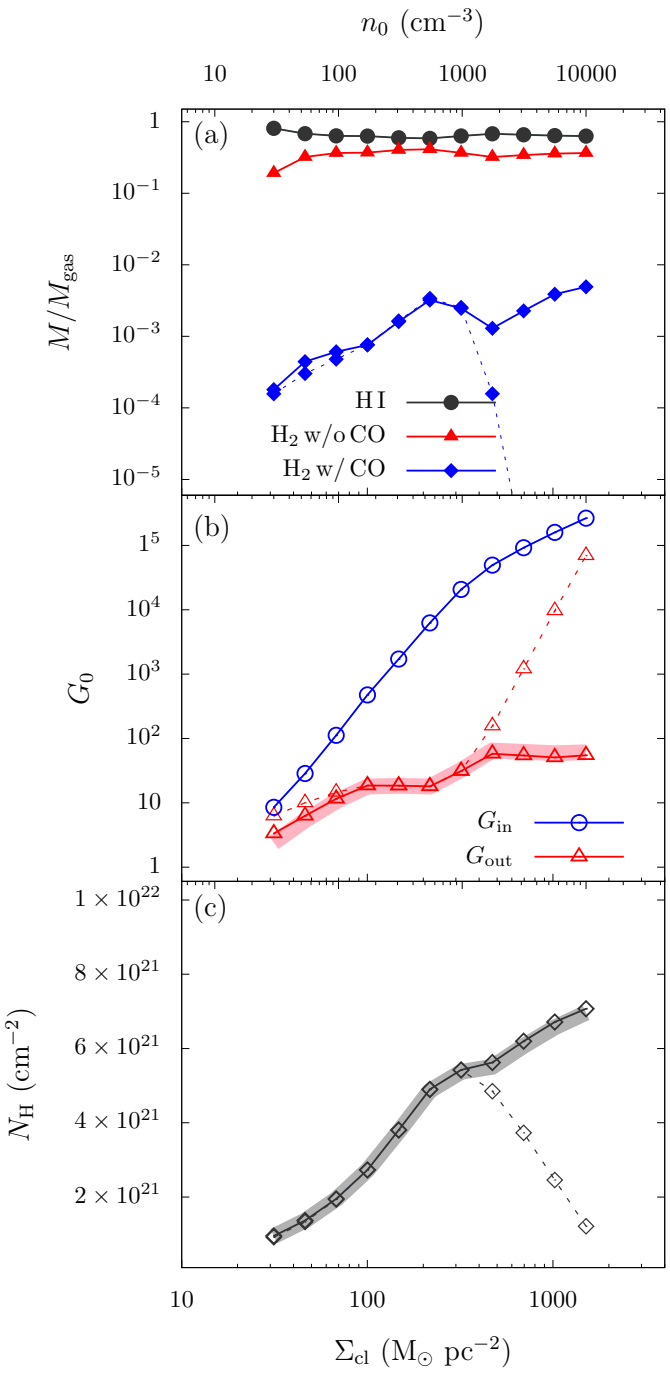

Figure 2.7: Chemical compositions of the gas that has not been converted into stars (molecular cloud "remnants"', panel a) and relevant quantities (panel b and c). The same cloud mass of $M_{\rm cl} = 10^5$ M$_\odot$ is assumed for the different cloud surface densities $\Sigma_{\rm cl}$ as in Fig. 2.5. *Panel (a):* the mass fractions relative to the total remnant mass $M_{\rm gas} = M_{\rm cl}(1-\varepsilon) - M_{\rm H\,II}$ for the different chemical properties: H I (black filled circles), H_2 without CO (red filled triangles), and H_2 with CO (blue filled squares). *Panel (b):* FUV fluxes throughout the shell. The blue open circles represent the incident FUV flux at the ionization front, and the red open triangles represent that at the preceding shock front. *Panel (c):* The hydrogen column density of the shell. In each panel, the symbols connected by the solid lines represent the cases where the minimum SFEs are limited by the EUV and FUV feedback. We also show the cases only with the EUV feedback with the thin symbols connected by the dashed lines. In panels (b) and (c), the thick solid lines represent the analytic evaluations of $G_{\rm out}$ and $N_{\rm H}^{\rm shell}$ by equations (2.33) and (2.32).

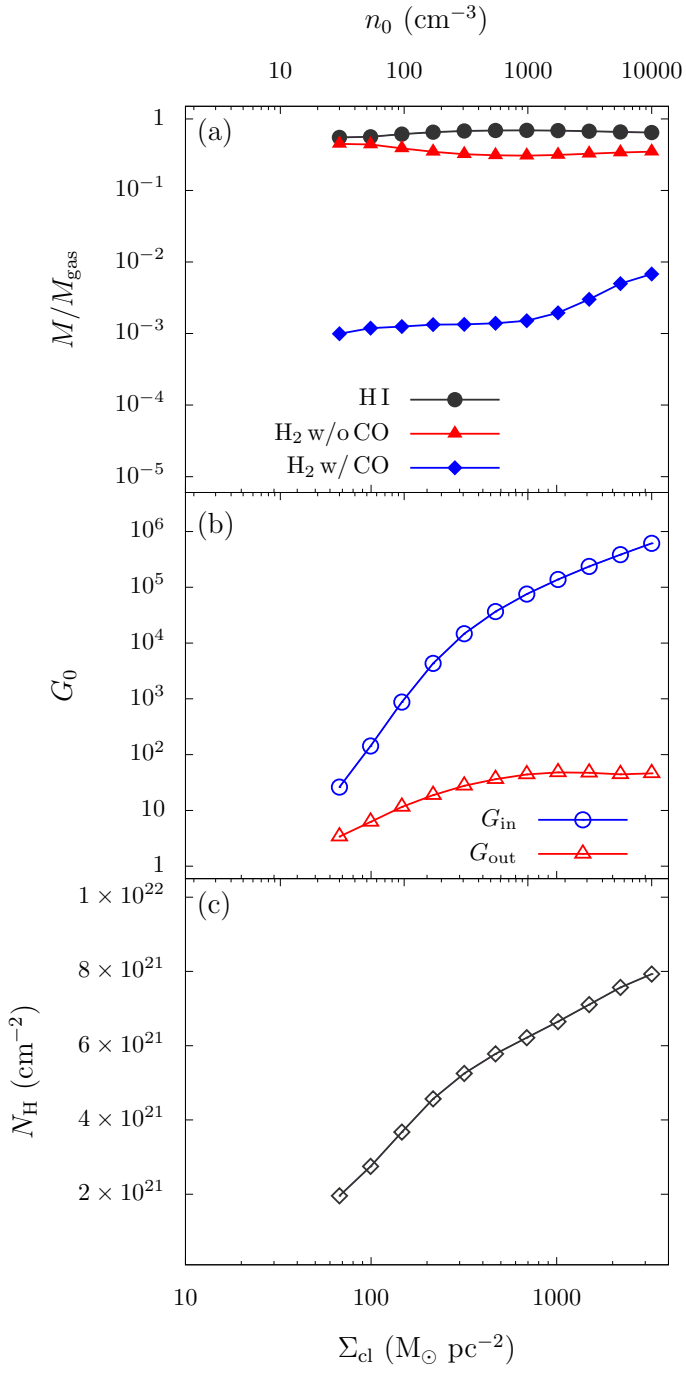

Figure 2.8: Same as Fig. 2.7 but for the higher cloud mass of $M_{\rm cl} = 10^6$ M$_\odot$. In the top panel, the H_2-with-CO fraction for the cases only with the EUV feedback is not presented because it is far below 10^{-5}.

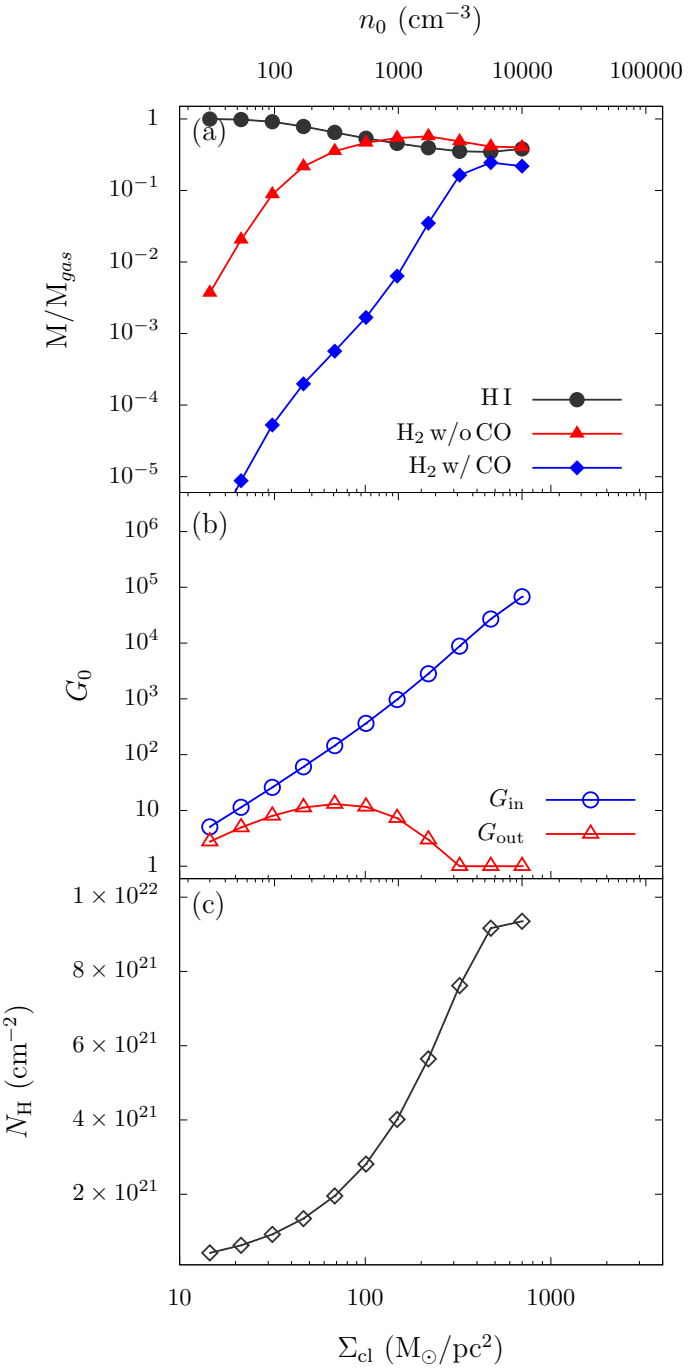

Figure 2.9: Same as Fig. 2.7 but for the lower cloud mass of $M_{\rm cl} = 10^4$ M$_\odot$. We here do not present the cases only with the EUV feedback unlike Figs. 2.7 and 2.8, because the resulting minimum SFE is exactly the same (see Section 2.2.2).

H_2 molecules associated with CO molecules and those without CO. The H_2 gas without CO molecules is the so-called "CO-dark" molecular gas. Let us see the cases where the minimum SFE is limited by the EUV and FUV feedback (Criterion 2, solid lines). Fig. 2.7 (a) shows that most of the H_2 molecules contained in the remnants are actually CO-dark. Such a trend only has a weak dependence on $\Sigma_{\rm cl}$; the mass of the CO-dark H_2 gas is generally much less than 10 % of that of the H_2 gas associated with CO molecules. This is caused by the different shielding processes of H_2 and CO molecules. As shown in Fig. 2.7(c), the column density of the shell is roughly $N_{\rm H}^{\rm shell} \simeq 2 - 7 \times 10^{21}$ cm^{-2}, corresponding to $A_V \simeq 1 - 3.5$. The dust attenuation of the FUV radiation is not very efficient for such cases. In fact, Fig. 2.7(b) shows that the FUV flux at the shock front $G_{\rm out}$ is several to several tens, which is high enough to photodissociate CO molecules. On the other hand, H_2 molecules are protected against the FUV radiation by the self-shielding effect even with the small column densities. Since the self-shielding is not available for CO molecules, which only have the small abundance, CO molecules are selectively destroyed.

We also investigate how the above properties are altered when we only consider the EUV feedback (see the thin symbols connected with dashed lines in Fig. 2.7). For such cases, only the quantities for $\Sigma_{\rm cl} \gtrsim 300$ M$_\odot$pc^{-2} are modified. Fig. 2.7(a) shows that the amount of H_2 with CO molecules are further reduced for such large $\Sigma_{\rm cl}$. Fig. 2.7(c) explains it is caused by the decline of the shell column density $N_{\rm H}^{\rm shell}$. We see that $N_{\rm H}^{\rm shell}$ rather turns to decrease with $\Sigma_{\rm cl}$ for $\Sigma_{\rm cl} \gtrsim 300$ M$_\odot$pc^{-2}. Fig. 2.7(b) shows that $G_{\rm out}$ accordingly rises with $\Sigma_{\rm cl}$, resulting in the efficient dissociation of CO molecules.

The above dependence on the feedback criteria is actually well understood with the following analytic arguments. Since the ionized gas density (at $t = t_{R_{\rm cl}}$) is given by

$$n_{\rm H\,II} = \sqrt{\frac{3 S_{\rm EUV} f_{\rm ion}}{4\pi R_{\rm cl}^3 \alpha_{\rm B}}}, \tag{2.28}$$

the mass of the ionized gas can be written as

$$\begin{aligned} M_{\rm H\,II} &= \frac{4}{3}\pi R_{\rm cl}^3 \mu_{\rm H} n_{\rm H\,II} \\ &= \mu_{\rm H} \left(\frac{4 f_{\rm ion} \Xi_{\rm EUV}}{3\alpha_{\rm B}\pi^{1/2}}\right)^{1/2} \varepsilon^{1/2} M_{\rm cl}^{5/4} \Sigma_{\rm cl}^{-3/4} \qquad (2.29) \\ &= 1.2 \times 10^4 \ M_\odot \left(\frac{\varepsilon}{10^{-2}}\right)^{1/2} \left(\frac{M_{\rm cl}}{10^5 \ M_\odot}\right)^{5/4} \left(\frac{\Sigma_{\rm cl}}{10^2 \ M_\odot {\rm pc}^{-2}}\right)^{-3/4}. \qquad (2.30) \end{aligned}$$

Since the ratio $M_{\rm H\ II}/M_{\rm cl}$ depends only weakly on $M_{\rm cl}$ and $\Sigma_{\rm cl}$, we take $M_{\rm H\ II} \sim 0.1\ M_{\rm cl}$. Then, the shell column density $N_{\rm H}^{\rm shell}$ and FUV flux at the shock front $G_{\rm out}$ obeys the following relations

$$M_{\rm shell} = M_{\rm cl}(1-\varepsilon) - M_{\rm H\,II} \approx 4\pi R_{\rm cl}^2 \mu_{\rm H} N_{\rm H}^{\rm shell}. \tag{2.31}$$

That is, we have

$$N_{\rm H}^{\rm shell} = \frac{\Sigma_{\rm cl}}{4\mu_{\rm H}}\left(1-\varepsilon-\frac{M_{\rm H\,II}}{M_{\rm cl}}\right) \sim \frac{\Sigma_{\rm cl}}{4\mu_{\rm H}}(0.9-\varepsilon), \tag{2.32}$$

$$G_{\rm out} = \frac{1}{F_{\rm H}}\frac{S_{\rm FUV}}{4\pi R_{\rm cl}^2}\exp(-\sigma_{\rm d}N_{\rm H}^{\rm shell}) \sim \frac{\varepsilon\Xi_{\rm FUV}}{4F_{\rm H}}\Sigma_{\rm cl}\exp\left[-\frac{\sigma_{\rm d}}{4\mu_{\rm H}}\Sigma_{\rm cl}(0.9-\varepsilon)\right]. \tag{2.33}$$

The factor of $(0.9-\varepsilon)$ in the above equations is actually important to understand the results. Fig. 2.5(a) shows that, for $\Sigma_{\rm cl} \gtrsim 300$ M$_\odot$pc^{-2}, $\varepsilon_{\rm min}$ only slightly changes with whether the FUV feedback is included or not. Since $\varepsilon_{\rm min}$ is close to 0.9, however, the resulting change of $(0.9-\varepsilon)$ is large. Only with the EUV feedback $(0.9-\varepsilon)$ significantly declines, meaning that there is only little amount of the remnant gas that shields the FUV radiation. If follows that the shell column density declines for $\Sigma_{\rm cl} \gtrsim 300$ M$_\odot$pc^{-2} for such cases.

We have performed the same analyses as above also for the cases with the different cloud masses $M_{\rm cl} = 10^6$ M$_\odot$ and 10^4 M$_\odot$. Fig. 2.8 presents the former cases with the large cloud mass 10^6 M$_\odot$. Again, most of the hydrogen molecules contained in the cloud remnants are not associated with CO molecules (Fig. 2.8a). If we only consider the EUV feedback, we can hardly find CO molecules remained. The shell column density $N_{\rm H}^{\rm shell}$ is only less than 2×10^{21} cm^{-2} (panel b), and the dust attenuation hardly contributes to reduce the FUV flux throughout the remnant gas (panel c).

Similarly, Fig. 2.9 presents the cases with the low-mass clouds with $M_{\rm cl} = 10^4$ M$_\odot$. Recall that the minimum SFE does not depend on whether the FUV feedback is considered or not for this case. We see the higher fractions of H_2 gas associated with CO molecules than the previous cases, in particular, for $\Sigma_{\rm cl} \gtrsim 300$ M$_\odot$pc^{-2} (panel a). The above analytic formulae are again useful to interpret such a variation. Since $\varepsilon_{\rm min} \ll 1$ for the current cases (see equation 2.24), the factor of $(0.9-\varepsilon)$ is just regarded as a constant. The combination of equations (2.32) and (2.33) leads to $N_{\rm H,shell} \propto \Sigma_{\rm cl}$ and $G_{\rm out} \propto \epsilon\Xi_{\rm FUV}\exp(-\Sigma_{\rm cl})$, indicating that the FUV flux rapidly drops with increasing $\Sigma_{\rm cl}$ because the shell column density increases. Indeed, the column density $N_{\rm H,shell}$ monotonically increases with increasing $\Sigma_{\rm cl}$ (panel c). The FUV flux $G_{\rm out}$ decreases in concert, as predicted by equation (2.33). For $\Sigma_{\rm cl} \gtrsim 300M_\odot$pc^{-2}, $G_{\rm out}$ is just limited by the background value $G_{\rm out} = 1$ (panel b). The above facts suggest that the FUV radiation from the cluster is substantially attenuated by the dust grains. As a result, a certain amount of CO molecules survives, being protected against the dissociating photons.

2.3 Discussion

2.3.1 Validity of thermal and chemical equilibrium

We have assumed the thermal and chemical equilibrium in our modeling. We here examine the validity of such assumptions. In order to do that, we evaluate the timescales over which

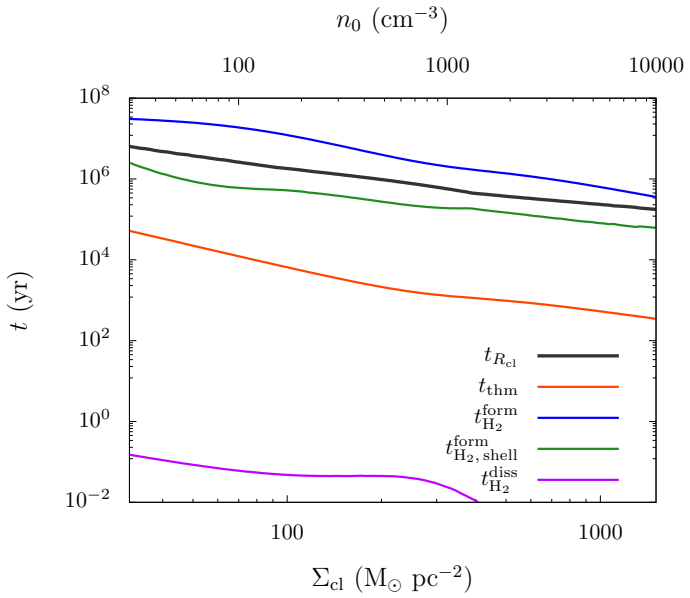

Figure 2.10: Comparisons of various characteristic timescales in our calculations with $M_{\rm cl} = 10^5$ M$_\odot$ and different cloud surface density $\Sigma_{\rm cl}$. The snapshots when the minimum SFE is determined with our Criterion 2 are used. Presented are the shell expansion timescale $t_{R_{\rm cl}}$ (black line), cooling time at the cloud edge (at $r = R_{\rm cl}$, red line), H_2 formation time at the cloud edge (blue line) and on the shell (green line) and H_2 dissociation time at cloud edge (purple line). The average shell density is calculated by equation (2.37.)

the thermal and chemical equilibrium states are achieved, $t_{\rm thm}$ and $t_{\rm chem}$. In particular, we consider the H_2 equilibrium timescale $t_{\rm H_2}$ as $t_{\rm chem}$ because its formation reaction on the grain surface is slowest among the included reactions. We calculate $t_{\rm thm}$ and $t_{\rm H_2}$ by the same method as in Koyama & Inutsuka (2000).

$$t_{\rm thm} = e/\Gamma, \tag{2.34}$$
$$t_{\rm H_2}^{\rm form} = x_{\rm H_2}/R_{\rm H_2}^{\rm form}, \tag{2.35}$$
$$t_{\rm H_2}^{\rm diss} = x_{\rm H_2}/R_{\rm H_2}^{\rm diss}. \tag{2.36}$$

where $R_{\rm H_2}^{\rm form}$ and $R_{\rm H_2}^{\rm diss}$ are the formation and dissociation rates of H_2 molecules, respectively (see equation 2.15). We use the snapshots at the epochs when the expanding shell reaches the cloud edge at $r = R_{\rm cl}$, i.e., $t = t_{R_{\rm cl}}$, where the expansion timescale $t_{R_{\rm cl}}$ corresponds to the dynamical timescale. The input parameters for calculation are $n = n_0$, $G_0 = G_{\rm out}$, and $N_{\rm H} = N_{\rm H}^{\rm shell}$ [Fig. 2.10 (b) and (c)]. Inside shell, in contrast, average density is

$$\bar{n} = N_{\rm H}^{\rm shell}/dR, \tag{2.37}$$

where $dR = r_{\rm sh} - r_{\rm IF}$ is geometrical thickness of the shell, while G_0 and $N_{\rm H}$ are the same as those in the outside the shell (this treatment is not so accurate, but is a reasonable approximation).

In Fig. 2.10 we present the above timescales as functions of $\Sigma_{\rm cl}$ for the cases with $M_{\rm cl} = 10^5$ M$_\odot$. We see that all the timescales gradually decrease with increasing $\Sigma_{\rm cl}$. The

dynamical timescale $t_{R_{\rm cl}} \propto R_{\rm cl}/c_{\rm s,H\ II}$ decreases, because the higher $\Sigma_{\rm cl}$ is the smaller becomes the cloud size for a fixed cloud mass (equation 2.1). The chemical and thermal timescales also drop because collisions, which drive the dominant cooling and chemical processes, occur more efficiently with the higher density. The figure shows that the thermal equilibrium timescale is always much shorter than the dynamical time, thus supporting our assumption of the thermal equilibrium.

The chemical equilibrium should hold within the dense shell, which carries most of the remnant gas, since the H_2 formation timescale is comparable to or shorter than the dynamical time $t_{R_{\rm cl}}$ (see the green line). By contrast, the H_2 formation timescale is somewhat longer than $t_{R_{\rm cl}}$ at the cloud edge (see the blue line). It means that the chemical equilibrium of H_2 molecules may not be achieved in the un-shocked ambient medium outside of the shell by the end of the calculations. However, the clouds we consider are initially fully molecular so that the chemical equilibrium should always be a good assumption even for H_2, since the dissociation timescale is much shorter than the formation timescale (see the purple line). Therefore our conclusion on the chemical composition presented in Section 2.2.3 will not change much even if we include the non-equilibrium effects.

2.3.2 Effects ignored

As already mentioned in Section 2.1.4, our 1D models of the PDR use assumptions for simplicity, e.g., the optically thin fine-structure line cooling and constant dust temperature throughout a PDR. In order to examine the validity of our treatments, we have also calculated the dynamical evolution of an H II region and surrounding PDR using a 1D radiation-hydrodynamics (RHD) code developed in Hosokawa & Inutsuka (2006) for several representative cases. The RHD code takes the effects ignored in the semi-analytic models into account, such as the trapping effect of the line emission and variable dust temperature. We have confirmed that the simulation results show the similar overall structure of the PDR as provided by the semi-analytic models in spite of the numerous differences. For instance, the evolution of the average density within the shell only differs by a few $\times$ 10 % between the RHD simulations and the semi-analytic models.

Although our RHD simulations and semi-analytic models employ the same method of Nelson & Langer (1999) for the CO formation rate, there are differences in evaluating the CO photodissociation rate. The semi-analytic models only use the FUV intensity G_i, for which the dust attenuation law is given by the cross section $\sigma_{\rm d} = 10^{-21}$ cm^{2}H^{-1}, to evaluate the CO dissociation rate. The RHD simulations, on the other hand, consider another FUV component only representing the CO dissociating band, for which the dust cross section is somewhat larger than the averaged value for the full FUV range 6 eV $\leq h\nu \leq$ 13.6 eV. Moreover, the RHD simulations also incorporate the effects of self- and H_2-shielding of CO molecules against dissociating photons (e.g., van Dishoeck & Black 1988). The semi-analytic models thus tend to overestimate the CO photodissociation rate, ignoring these effects. In order to evaluate this effect, we have compared the simulation and model results for the case with $M_{\rm cl} = 10^5$ M$_\odot$ and surface density $\Sigma_{\rm cl} = 300$ M$_\odot$pc^{-2} (e.g., see Figs. 2.4 for the model). As shown in Figure 2.7, the model predicts that only $\sim$ 0.1 % of the cloud remnant should be H_2 molecular gas associated with CO molecules. The RHD simulation run with the same

setting shows that this quantity is ~ 1 % at the epoch when the expanding shell reaches the cloud edge, $t \simeq 6 \times 10^5$ years since the birth of the H II region. We interpret that such a high value in the simulation run is due to the CO dissociation rate overestimated in the model. If we ignore the effects which are not considered in the model, the simulation returns the lower value ~ 0.03 %. We have also found that the value rapidly rises in the corresponding stage, varying by an order of magnitude in $\sim 10^5$ years. We conclude that, while there is the general trend that most of the molecular gas contained in the cloud remnants should be CO-dark, the exact amount of the CO-bright molecular gas is difficult to be accurately estimated. Nonetheless, it would be intriguing to investigate how the dispersing clouds are to be observed as a time sequence. For that purpose, C atoms rather than CO molecules are a more useful tracer of the CO-dark gas because of the higher abundance (e.g., Li et al. 2018). Coupling an extended chemistry network beyond the approximation method by Nelson & Langer (1999) with time-dependent hydrodynamics simulations should provide such predictions.

2.3.3 Other stellar feedback processes

In order to isolate potential roles of the FUV feedback during the cloud disruption, we have employed the simple assumption on the H II bubble expansion, i.e., that the thermal pressure excess of the photoionized gas with respect to the ambient medium drives the expansion. As briefly noted in Section 2.1.3, theoretical studies suggested that radiation pressure exerted on the shell affects the expansion motion (e.g., Krumholz & Matzner 2009; Fall et al. 2010; Murray et al. 2010; Kim et al. 2016). Such studies all show that the expansion is mainly driven by the radiation pressure rather than the gas pressure if $\Sigma_{\rm cl} \gtrsim 100$ $\mathrm{M_\odot pc^{-2}}$, which is also confirmed by recent numerical simulations, although for turbulent clouds the transition occurs at somewhat higher $\Sigma_{\rm cl}$ (e.g., Kim et al. 2018). Kim et al. (2016) have actually incorporated the effect of the radiation pressure in their model by taking $F_{\rm rad} = L/c$ as the average radiation force. We also follow the same approach as theirs to modify the temporal evolution of the shell radius given by equation (2.12). The resulting minimum SFEs for such cases are also presented by the blue dashed line in Fig. 2.5(b), for which only the EUV feedback is assumed (Criterion 1) with $M_{\rm cl} = 10^6$ $\mathrm{M_\odot}$. We find that the radiation pressure effect further reduces $\varepsilon_{\rm min}$, and that its effect is more prominent for the higher $\Sigma_{\rm cl}$. Inversely, the FUV feedback are effective for the low surface density $\Sigma_{\rm cl} \lesssim 100$ $\mathrm{M_\odot pc^{-2}}$ (Section 2.2.2), for which the effect of the radiation pressure is limited.

Stellar winds from high-mass stars are also omitted in our models, though they have been referred to as the main driver of the bubble around a massive cluster including many O-type stars (e.g., McKee et al. 1984). The dynamics of the wind-driven bubbles has been modeled assuming the spherical symmetry (e.g., Weaver et al. 1977), and it is well described by an expansion law which differs from equation (2.12). Recent studies further investigate the interplay between the radiation pressure and stellar winds during the bubble expansion (e.g., Rahner et al. 2017, 2019). Since we have focused on the FUV feedback based on the model of Kim et al. (2016), we have ignored the wind effects following their approach. Regarding the minimum SFEs, we have shown that the FUV feedback is effective for massive GMCs with $M_{\rm cl} \gtrsim 10^5$ $\mathrm{M_\odot}$ (Section 2.2.2). The stellar winds may affect the bubble dynamics

for such cases, where the birth of massive clusters with $\gtrsim 10^3$ $M_\odot$ is supposed assuming $\varepsilon \sim 0.01$. We have also shown that the FUV radiation produces the CO-dark gas even for the less massive clouds with $M_{\rm cl} \lesssim 10^5$ $M_\odot$ (Section 2.2.3). The star cluster considered is relatively small with a few O-type stars at most, for which the wind effect should be limited. In any rate, recent studies point out that the wind effects on the bubble expansion should be overestimated in 1D modeling. Multi-dimensional simulations show that the hot gas generated in the wind-driven bubble actually quickly leaks out through low-density channels rather than being confined (e.g., Rogers & Pittard 2013). There are no clear observational signatures that the bubble expansion is evidently driven by the winds (e.g., Lopez et al. 2014). We note that multi-dimensional effects should also affect the H II bubble dynamics even without the wind effects, which is further discussed in Section 2.3.4.

In this paper, we have considered the stellar feedback on GMCs before the first supernova explosion occurs. As presented in Fig. 2.10, the dynamical timescale of an H II bubble expansion is longer for the lower cloud surface density, $\simeq$ several $\times$ Myr for $\Sigma_{\rm cl} \lesssim 100$ $M_\odot {\rm pc}^{-2}$. This is still shorter than the lifetime of high-mass stars that cause the supernova explosions ~ 10 Myr, but there may not be a long time lag. It is interesting to speculate what happens if a supernova explosion occurs within a clouds under the stellar FUV feedback. Since the supernova explosion add mechanical feedback on the cloud, it further contributes to reducing the SFE. Moreover, shock waves around the expanding supernova remnant sweep up the gas of the cloud being destroyed, which contains the CO-dark gas under the FUV feedback. Since the shock compression is a possible channel of the molecular cloud formation (e.g. Inoue & Inutsuka 2008, 2009), the CO-dark gas may be brought back into "CO-bright" molecular phase once the FUV radiation is somehow attenuated. Note that key chemical reactions producing CO molecules near the supernova remnants should differ from those in normal star-forming environments (e.g., Bisbas et al. 2017).

2.3.4 Inhomogeneous cloud density structure

In our one-dimensional semi-analytic modeling, we have assumed the homogeneous density distribution within a molecular cloud. It is actually possible to relax such an assumption by improving our current model. Kim et al. (2016) have also considered cases with the power-law density distributions $\rho \propto r^{-w}$ with $w < 1.5$. In general, the photoionized gas expands more rapidly with the less efficient "trapping" for the cloud with the steeper density gradient (e.g., Franco et al. 1990). An extreme case is known as the "champagne flow" or "blister-type" H II regions (e.g., Tenorio-Tagle 1979), for which the gas motion is not adequately described as the pressure-driven expanding shell, but rather as the photoevaporation where the ionized gas freely escapes from the cloud. Fully investigating the FUV feedback with such a variety of dynamical evolution is out of scope of the current work, but further studies are warranted (e.g., Hosokawa 2007; Geen et al. 2019).

In order to consider the more realistic clumpy cloud structure, one has to resort to 3D radiation-hydrodynamics numerical simulations. A number of authors in fact have conducted such simulations mostly focusing on the stellar EUV feedback (e.g., Walch et al. 2012, see also Section 1). Simulations by Kim et al. (2018) have followed the EUV feedback againt clumpy and turbulent GMCs to drive SFEs as functions of the cloud masses and surface

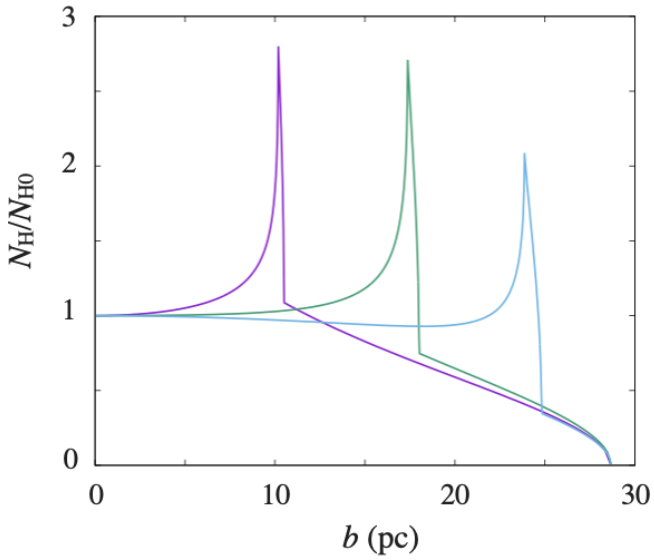

Figure 2.11: Shell column density at b pc from bubble center. The value is normalized by the center value $N_{H,0}$. The model is the case with $n_c = 300$ cm^{-3}, and each line shows the age with $t = 1.0$ Myr (purple line), 2.0 Myr (green line), and 3.0 Myr (blue line), respectively.

densities. They have confirmed the qualitative agreements with Kim et al. (2016)'s model predictions, but also found that the model underestimates minimum SFEs compared to the simulation results. The simulations show that the ionized gas escapes from a cloud through low-density parts and the actual feedback is dominated by photoevaporation of surviving clumps. The FUV feedback in the clumpy medium has yet to be fully studied by similar numerical approaches (e.g., Arthur et al. 2011). Although we just have assumed that the star formation is locally quenched in a warm PDR (Section 2.1.5), it should be also verified with such simulations. Note that the star formation might be rather induced in a clumpy PDR because pre-existing clumps exposed to the FUV radiation would be compressed via the radiation-driven implosion (e.g., Gorti & Hollenbach 2002; Walch et al. 2013, 2015; Nakatani & Yoshida 2018).

2.3.5 Comparison with infrared observations of H_2 shell in our Galaxy

As we have shown in Section 1.1, a large samples of H_2 molecular shells created around massive stars are available, for which our 1D semi-analytic models may be applicable. Below we present comparisons between our model predictions and statistical properties of the observed shells.

We refer to 182 Galactic H_2 bubble data from Palmeirim et al. (2017), which includes the data of number intensity of Lyman continuum (corresponding to $S_{\rm EUV}$), average shell density $\langle n_{\rm sh} \rangle$, radius of ionized region $r_{\rm IF}$, shell radius $r_{\rm sh}$, and shell mass $M_{\rm sh}$. Averaged shell profile is shown in Fig. 1.3. We calculated the evolution of shell dynamics and shell structure by using the 1D semi-analytic model constructed in Sec. 2.1, but without con-

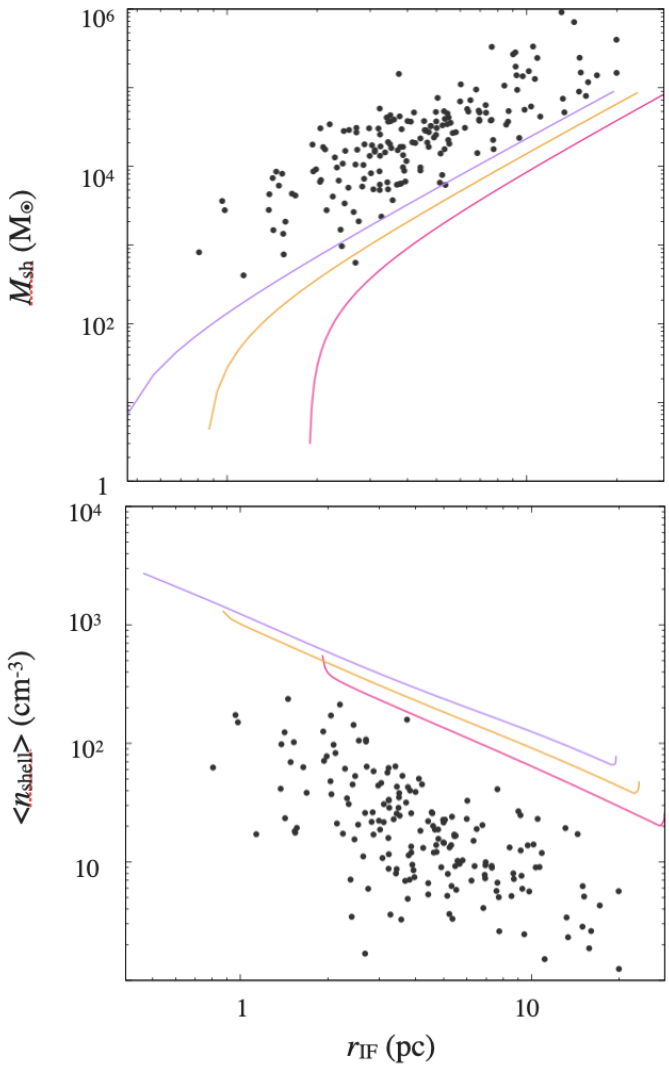

Figure 2.12: Shell mass $M_{\rm sh}$ (top) and averaged shell density $\langle n_{\rm sh} \rangle$ (bottom) at shell radius $r_{\rm IF}(t)$. Each line shows the model with $n_{\rm c} = 300$ cm^{-3} (pink line), 1000 cm^{-3} (orange line), and 3000 cm^{-3} (purple line), respectively. The black dots are the Galactic bubble data from Palmeirim et al. (2017).

sidering the cloud disruption criteria. We set initial central density of molecular clouds $n_c = 300, 1000, 3000$ cm^{-3} and EUV emission from star cluster $S_{\rm EUV} = 10^{49}$ s^{-1} as the input parameter. These values are chosen by the typical values from the observational data.

Fig. 2.11 shows the profile of the shell column density calculated by our model. The peak value of column density has $\sim 2-3\ N_{\rm H0}$ at $b \sim r_{\rm IF}(t)$, while $\sim 1.2\ N_{\rm H,0}$ in observation. We also find that 1D model predicts "thin" shell structure while observations show "thick" shell (see Fig. 1.3 rihgt).

Fig. 2.12 shows the time evolution of shell mass and averaged shell density. Although rough tendency is consistent, the shell masses in our model are systematically too small when compared with observational data.

These results show that there would be some reasons for shells to have "thick" structure by missing 3D effects in 1D semi-analytical model. For example, actually the shells have clumpy structure, so shells are heated more by EUV and FUV radiation. As a result, our 1D semi-analytical model can represent only the rough tendency of the shell structure, however, detailed 3D simulations are needed for more realistic models.

Chapter 3

Observational signatures of massive star-cluster forming regions

In this chapter, we discuss the observational signatures of massive star-cluster forming regions based on the 3D RHD simulations by Fukushima & Yajima (2021).

3.1 Limitations of 1D semi-analytic model

Our 1D semi-analytic model provides a simple framework to predict the SFE of GMCs (see Chapter 2), but it also suffers from various limitations. For example, internal structure of molecular clouds is often neglected in 1D models. Also, 1D modeling can not predict the properties of newborn star clusters, such as spatial stellar distributions. A related issue is that 1D model cannot clarify the origin of the observed diversity of star clusters because their formation process is neglected in the model. It is also difficult to investigate the observational signatures of cluster-forming clouds by 1D model. Since we do not consider the gas accretion toward the star cluster, such gas dynamics is beyond our simple 1D modeling.

To sum up, observations show multi-dimensional features (see Section 1.2), which cannot be described by our simple 1D model. We summarize the limitation of simple 1D model in Table 3.1. Then, numerical 3D RHD simulation allows us to develop more realistic models that cannot be considered in 1D models. Recently, such realistic modeling of the star cluster formation and destruction of the molecular clouds is becoming feasible (e.g. Fukushima & Yajima 2021, see also Section 1.2), however, synthetic observation is also necessary to verify such simulation results observationally. Now we investigate the observational signatures of GMCs forming YMCs. We calculate the CO, [C II], and [O I] line emissions from star-forming clouds and the velocity distribution of cluster gas on the near side by using the results from Fukushima & Yajima (2021) and compare them with the simulation results.

3.2 Methodology

3.2.1 Simulation models in Fukushima & Yajima (2021)

Fukushima & Yajima (2021) perform the three-dimensional hydrodynamics simulations with

Table 3.1: Treatment in theoretical model

	1D semi-analytic model	3D RHD simulation
Internal structure	Spherical and isotropic	Turbulent and inhomogeneous
Cluster properties	Single cluster at the center	Spatial stellar distribution
Duration of star formation	Instantaneous	Continuous

radiative transfer (RT) into an adoptive mesh refinement code, SFUMATO (Matsumoto et al. 2015), which is dubbed SFUMATO-M1. They develop the RT module based on the moment equations with the M1-closure. Below we briefly describe their simulation method and models.

In Fukushima & Yajima (2021), they set the size of calculation boxes as three times the cloud radius ($R_{\rm cl}$) on a side. The maximum refinement level is fixed at $l_{\rm max} = 4$ and the minimum cell size is $\Delta x = 0.059$ pc. The simulations end at when 4× free-fall time ($t_{\rm ff}$) elapses. The hydrodynamics is solved with Cartesian coordinate. They solve the following basic equations of compressible hydrodynamics:

$$\frac{\partial \rho}{\partial t} + \nabla(\rho \boldsymbol{v}) = 0, \tag{3.1}$$

$$\frac{\partial \rho \boldsymbol{v}}{\partial t} + \nabla(\rho \boldsymbol{v} \otimes \boldsymbol{v}) + \nabla P = \rho(\boldsymbol{g} + \boldsymbol{f}), \tag{3.2}$$

$$\frac{\partial \rho E}{\partial t} + \nabla[(\rho E + P)\boldsymbol{v}] = \rho(\boldsymbol{g} + \boldsymbol{f}) \cdot \boldsymbol{v} + \Gamma - \Lambda, \tag{3.3}$$

where E is total energy defined as

$$E = \frac{|\boldsymbol{v}|^2}{2} + (\gamma - 1)^{-1} \frac{P}{\rho}, \tag{3.4}$$

$\rho, P, \boldsymbol{v}, \boldsymbol{g}, \Gamma$, and Λ are density, pressure, velocity, gravitational force, the heating and cooling functions. They estimate the adiabatic exponent γ as in Omukai & Nishi (1998). In equations (3.2) and (3.3), $\boldsymbol{f}$ represents the radiation pressure force. They consider radiation pressure of EUV photons absorbed by Hi and dust grains, and of FUV and IR photons absorbed by dust grains.

They take into account the chemical networks of 11 species: H^0, H_2, H^- , H^+ , H_2^+, e, CO, C^+, O^0, O^+, and O^{2+} (see also Fukushima et al. 2020b). The number density of the i-th species is calculated as

$$\frac{\partial (x_i n_{\rm H})}{\partial t} + \nabla(x_i n_{\rm H} \boldsymbol{v}) = x_i n_{\rm H} R_i, \tag{3.5}$$

where $n_{\rm H}$ is the number density of hydrogen nuclei, $x_i = n_i / n_{\rm H}$ is the fractional abundance of each chemical species, and R_i is the reaction rate involving the i-th species. They adopt the simple chemical network of Nelson & Langer (1997) for CO formation, which has been used for the RHD simulations (e.g., Hosokawa & Inutsuka 2006). To obtain the relative abundances of O^0, O^+, and O^{2+}, they adopt the following procedure (see also Fukushima et al. 2020a). They assume that the ionization rate of O^0 is equal to that of H^0 because the

Table 3.2: Parameter set

Model	$M_{\rm cl}$ ($M_\odot$)	$\Sigma_{\rm cl}$ ($M_\odot$/pc^2)	$R_{\rm cl}$ (pc)	n_0 (cm^{-3})	$t_{\rm ff}$ (Myr)
Compact	10^6	400	28.2	309	2.5
Diffuse	10^6	100	56.4	38.6	7.0

ionization potential energies of O^0 and H^0 are similar. The abundances of doubly ionized oxygen are determined as the chemical equilibrium between O^+, and O^{2+}.

The heating and cooling processes considered include (1) the thermal processes related to the chemical reactions, (2) line cooling of H_2, [C II], CO, [O I], [O II], and [O III], and (3) energy transfer between gas and dust grains. As the radiative processes, we include heating of H^0 photoionization and H_2 photodissociation. The dust grain temperature is estimated from the energy balance between the absorption/emission of radiation and energy transfer with gas. The temperature floor at $T = 10$ K is adopted as in Fukushima et al. (2020b).

The conditions for the production of sink particle are as follows (Federrath et al. 2010): (1) the gas density is higher than the threshold value $\rho_{\rm thm}$; (2) the birthplace is the local minimum of gravitational potential; (3) the velocity divergence $\nabla \cdot \mathbf{v}$ and all the eigenvalues of the symmetric part of the velocity gradient tensor $\nabla \mathbf{v}$ are negative; (4) the sum of the thermal, kinetic and gravitational energy is negative. The density threshold is set as $\rho_{\rm thm} = 8.86 c_s^2/(\pi G \Delta x^2) = 9.3 \times 10^{-19} (R_{\rm cl}/20\ {\rm pc})^2$ g cm^{-3} (Gong & Ostriker 2013; Kim et al. 2018) where c_s is the sound speed, and $T = 20$ K is used here. They set a sink radius as $r_{\rm sink} = 2\Delta x$ and do not consider mergers among sink particles.

They regard each sink particle as a star cluster. To evaluate the luminosity and spectrum of the star cluster, they take the average of the stellar isochrone of Chen et al. (2015) and the Chabrier initial mass function (IMF, Chabrier 2003) with the stellar mass range from 0.1 to 150 $M_\odot$. In our simulations, the duration time of star formation is on the order of Myr, and thus we use their isochrone at $t = 1$ Myr. We assume that low-mass cluster particles with < 50 $M_\odot$ do not emit ionizing photons, neglecting the weak contributions from the smaller clusters.

3.2.2 Synthetic observational signatures by post-process calculations

We extract characteristic observational signatures expected with the different evolution described in Section 1.2. We compare the two different cases starting from the initial clouds with $M_{\rm cl} = 10^6$ $M_\odot$. One is the case with the cloud surface density $\Sigma_{\rm cl} = 400$ $M_\odot$/pc^2, where a YMC-like cluster appears (hereafter "Compact" model). The free-fall time for the initial cloud is $t_{\rm ff} \sim 2.5$ Myr. The other is the case with $\Sigma_{\rm cl} = 100$ $M_\odot$/pc^2, where only a less massive and diffuse cluster forms (hereafter "Diffuse" model). The corresponding free-fall time is $t_{\rm ff} \sim 7$ Myr. The model parameters are summarized in Table 3.2.

Fig. 3.1 presents the stellar mass and the bound fraction of the star cluster as a function of time. The total stellar mass reaches 0.1 of the cloud mass at $t \sim 1.3$ $t_{\rm ff}$ in the both case, however, the bound fraction shows quite different evolution between the two models. In the

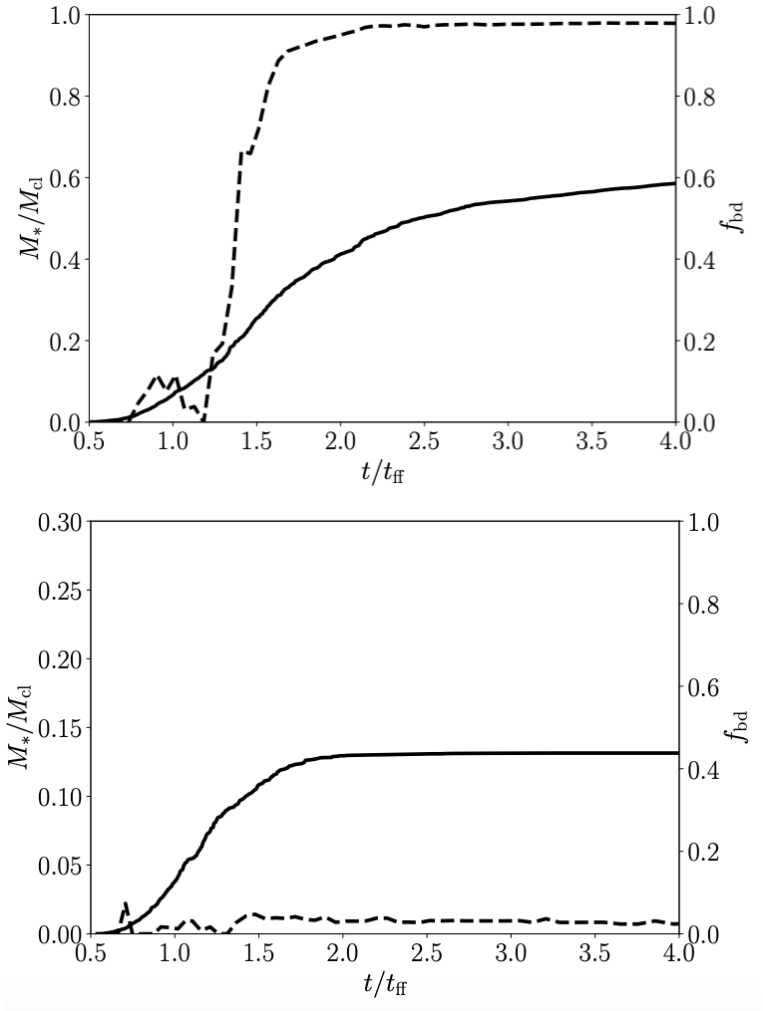

Figure 3.1: The time evolution of the stellar mass normalized by the initial cloud one and the bound fraction in the case with $(M_{\rm cl}, \Sigma_{\rm cl}) = (10^6\ {\rm M}_\odot,\ 400\ {\rm M}_\odot\ {\rm pc}^{-2})$ (upper panel) and $(M_{\rm cl}, \Sigma_{\rm cl}) = (10^6\ {\rm M}_\odot,\ 100\ {\rm M}_\odot\ {\rm pc}^{-2})$ (lower panel)

Compact model (shown in the upper panel of Fig. 3.1), the bound fraction exceeds 0.9 at $t \sim 1.5\ t_{\rm ff}$, and it is almost constant until the end of the simulation. The star formation rate (SFR) also starts to increase at $t \sim 1.3\ t_{\rm ff}$, and it continues until $t \sim 2.0\ t_{\rm ff}$. After that, radiative feedback slows down the star formation, but gas around the star cluster cannot disperse due to the deep gravitational potential. Thus, the star formation continues for a long time until $t \sim 3.5\ t_{\rm ff}$, finally resulting in the SFE of 0.7. In the Diffuse model (the lower panel of Fig. 3.1), however, the bound fraction is almost 0 throughout the simulation. The radiative feedback exceeds the gravitational force, thus the SFR starts to decreases at $t \sim 1.3\ t_{\rm ff}$ and almost terminates at $t \sim 1.5\ t_{\rm ff}$, finally resulting in the SFE of 0.15.

The data cube which we analyze is composed by $(128)^3$ cells. The cells homogeneously distribute in the whole computational domain, and they are different from the AMR cells used in the original simulation runs. We consider the three different directions of an observer, which along with x, y and z axes. We take $(128)^2$ lines of sight for each direction. We solve the level populations of CO molecules, C^+ ions, and O atoms at the cell centers as post-process calculations to get emissivity and absorption coefficients for CO $J = 1 - 0$, [C II] 157.7 μm, and [O I] 63.1 μm transitions. The line emissivity and absorption coefficients are given by

$$j_{ij} = \frac{h\nu_{ij}}{4\pi} n_i A_{ij} \phi_{ij}, \tag{3.6}$$

$$\alpha_{ij} = \frac{h\nu_{ij}}{4\pi} (n_j B_{ji} - n_i B_{ij}) \phi_{ij}, \tag{3.7}$$

where ν_{ij} is the photon frequency corresponding to the energy difference, n_i and n_j are the number density at the upper and lower energy levels i and j, A_{ij}, B_{ij}, and B_{ji} are the Einstein coefficients, and ϕ_{ij} is the line profile function taking the Doppler broadening into account (e.g. Hollenbach & McKee 1979). Then we get line emission map by solving the radiative transfer along each line of sight.

We also calculate the line-of-sight velocity map of the molecular gas in front of the cluster, supposing that the gas motion is detectable by means of the molecular absorption lines against the background radio continuum emission from an H II region (e.g. Sollins et al. 2005). To this end, we evaluate the mean velocity weighted by the column density of CO molecules:

$$\langle v_l \rangle = \frac{\int v_l n_{\rm CO}\ ds}{\int n_{\rm CO}\ ds}, \tag{3.8}$$

where we take the integration only over half of the computational domain in each direction. For instance, when we assume the observer is located at $x \to +\infty$ and the mass center of the cluster is on the y-z plane, the integration range is $x > 0$ along each line of sight. We consider different observers located at $x \to \pm\infty$, $y \to \pm\infty$, and $z \to \pm\infty$ in total, and we calculate six different velocity maps for a given simulation snapshot.

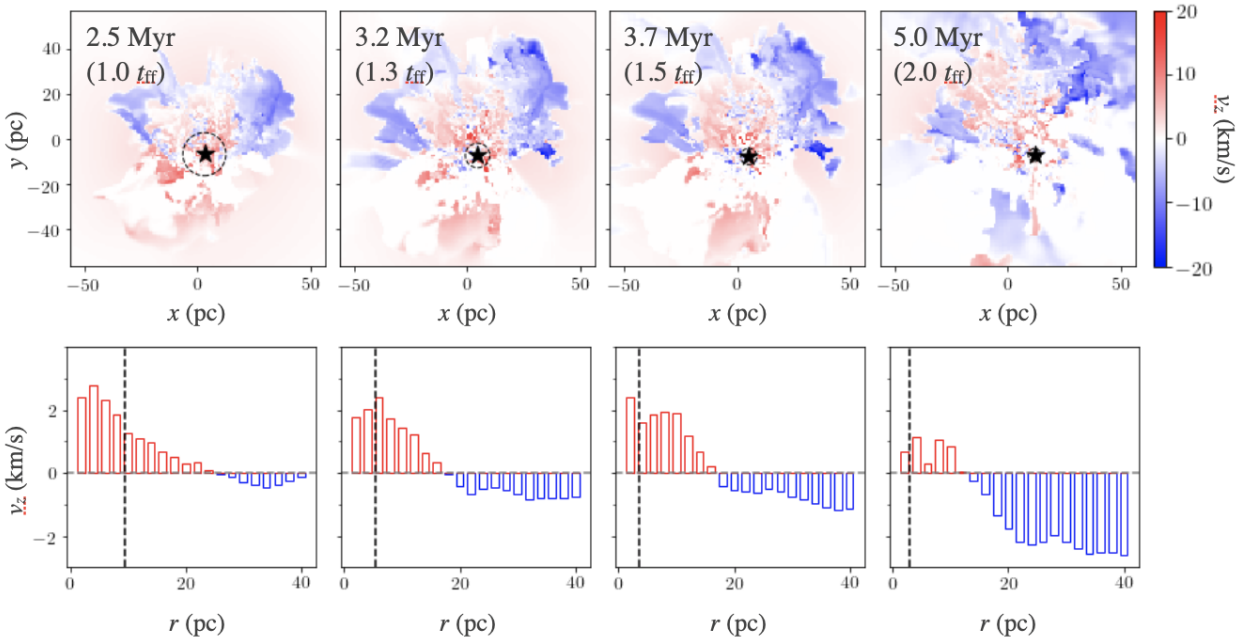

Figure 3.2: Velocity distribution of cluster gas on the near side of the cloud with ($M_{\rm cl}$, $\Sigma_{\rm cl}$) = (10^6 $M_\odot$, 400 $M_\odot$ pc^{-2}) at t = 2.5 (1.0 $t_{\rm ff}$), 3.2 (1.3 $t_{\rm ff}$), 3.7 (1.5 $t_{\rm ff}$) and 5.0 Myr(2 $t_{\rm ff}$). Red corresponds the infall motion for the center cluster. *Top:* $N_{\rm CO}$-weighted velocity distribution map of cluster gas on the near side. The gray star represents the position of the center of gravity of the cluster, and the gray dashed circle corresponds the half-mass radius of the cluster, respectively. *Bottom:* The circularly averaged velocity of molecular gas on the near side. The horizontal axis denotes the distance from the center of gravity of the cluster. The vertical dotted line indicates the half-mass radius of the cluster.

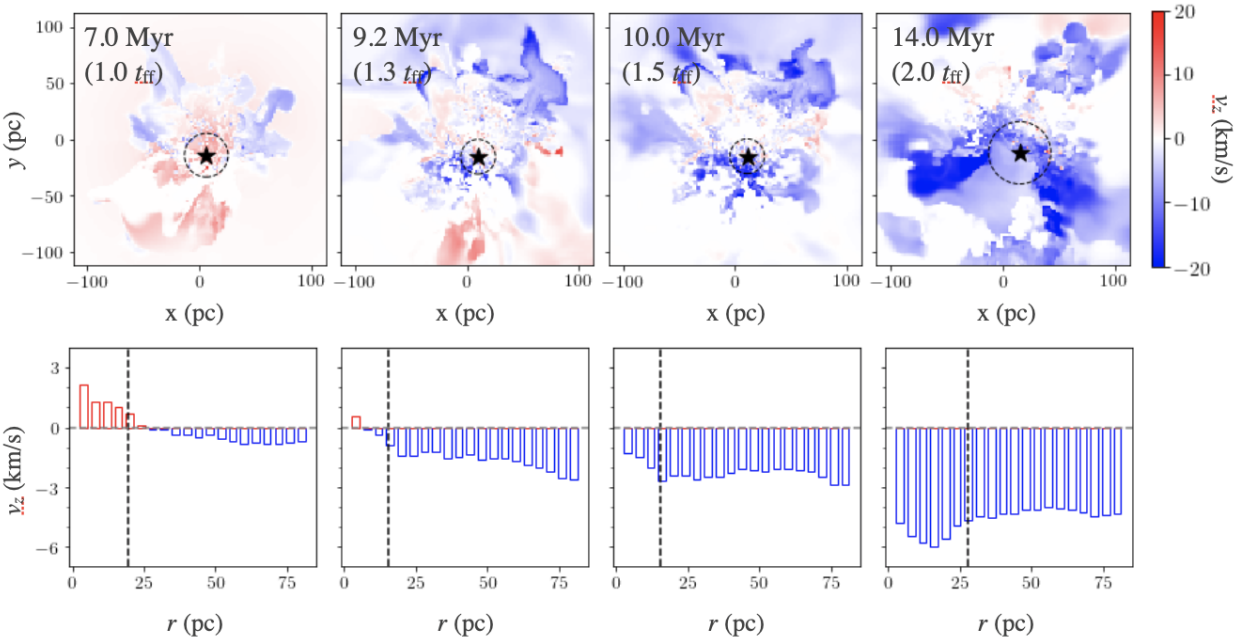

Figure 3.3: Same as Fig. 3.2, but for the case with $(M_{\rm cl}, \Sigma_{\rm cl}) = (10^6\ {\rm M}_\odot, 100\ {\rm M}_\odot\ {\rm pc}^{-2})$ at $t = 7.0$ (1.0 $t_{\rm ff}$), 9.2 (1.3 $t_{\rm ff}$), 10.0 (1.5 $t_{\rm ff}$) and 14.0 Myr(2 $t_{\rm ff}$).

3.3 Results: synthetic observational signatures

3.3.1 Velocity distribution of cluster gas on the near side

We show the time evolution of the $N_{\rm CO}$-weighted line-of-sight velocity map of cluster gas on the near side of the Compact model in Fig. 3.2. We calculate the averaged radial profiles of the velocity map by taking the points at the same distance from the cluster center and averaging their values. We find the infall motion with velocity 2 - 3 km/s into cluster center throughout the star-forming stage ($\sim 2.0\ t_{\rm ff}$). There are also outflow motion in outer region ($r \gtrsim 20$ pc). The region where the outflow is dominant gradually extends inward, and the outflow velocity increases: ~ 1 km/s at 1.5 $t_{\rm ff}$, and ~ 2 km/s at 2.0 $t_{\rm ff}$. As seen in the left panel of Fig. 1.8, there is infall motion near the cluster due to the gravitational binding of the gas, but outflow is dominant in the outer part of the cluster because the gas pressure due to the radiative feedback is more dominant than the gravitational force.

Fig. 3.3 shows the case with the Diffuse model. The first ~ 1.0 $t_{\rm ff}$ shows the similar signatures of infall motion as the Compact model, but after 1.3 $t_{\rm ff}$, when star formation ceases, outflow motions with the velocity of 2-3 km/s become dominant, and at 2.0 $t_{\rm ff}$, the outflow velocity exceeds 5 km/s. As seen in the right panel of Fig. 1.8, the effect of radiative feedback is more pronounced in the case where no YMC is formed, and the molecular cloud is dissipated by gas pressure.

3.3.2 Radial distributions of line emission around the cluster

To examine the difference in observational signatures between the two models, we compare the averaged radial profiles of the line emission map and the peak value. The averaged radial profile is calculated by the same method explained in Section 3.3.1.

In this section, we investigate the [C II] emission. Figs. 3.4 and 3.5 show the time evolution of [C II] emission map and its radial profile in Compact and Diffuse model. In the Compact model (Fig. 3.4), the closer to the center of the cluster, the brighter [C II] emission is. Especially $t \gtrsim 1.3\ t_{\rm ff}$, the central region tends to have a core-like structure, while the surrounding regions become flat profile. This is due to the strong gravitational force in the center, which traps the gas. In the Diffuse model (Fig. 3.5), on the other hand, while the profile at $1.0\ t_{\rm ff}$ is similar to that of the Compact model, the central strong emission declines by the epoch of $1.5\ t_{\rm ff}$. The radial profile becomes almost flat at $2.0\ t_{\rm ff}$. This evolution is caused by the dissipation of the molecular cloud by radiative feedback.

Fig. 3.6 shows the radial profiles of the [C II] emission of the case with the Compact model at $t = 1.5\ t_{\rm ff}$ and with the Diffuse model at $t = 1.0\ t_{\rm ff}$. These snapshots both present the gas infall motion toward the cluster center (Figs. 3.2 and 3.3). However, Fig. 3.6 suggests that the peak value and the radial profile of the [C II] emission is quite different. The Compact model shows the high peak intensity of [C II] emission and steep radial profile compared to the Diffuse model.

We also investigate the [O I] and CO emission, separately in Appendix A.

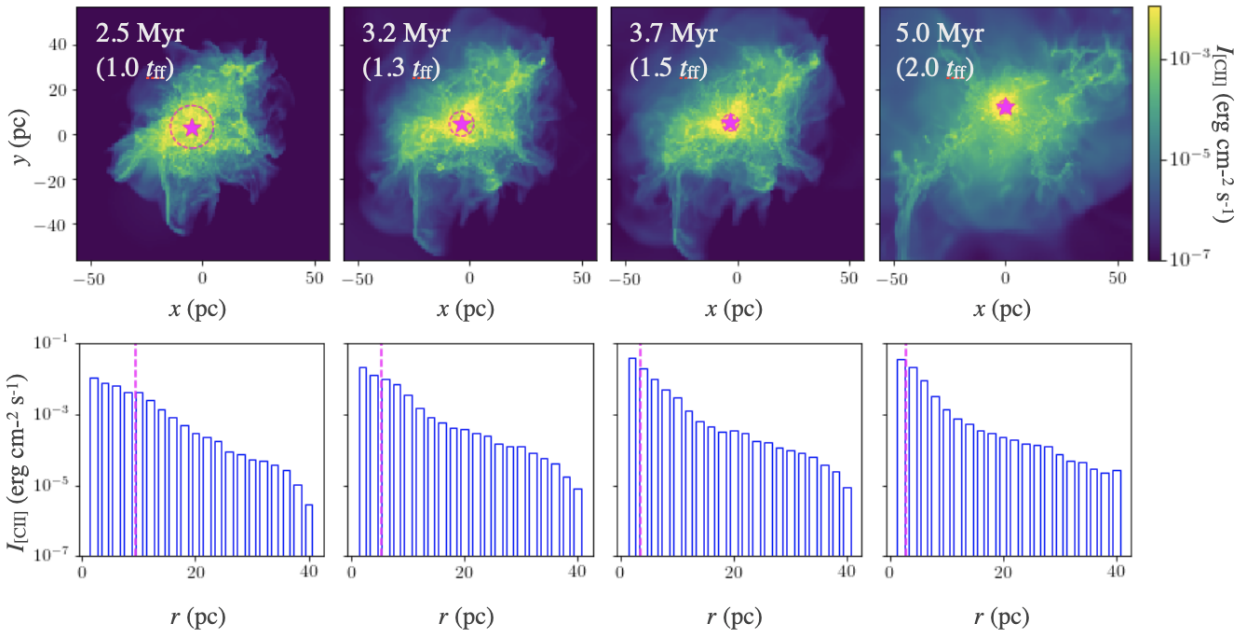

Figure 3.4: [C II] line emission maps of the cloud with ($M_{\rm cl}$, $\Sigma_{\rm cl}$) = (10^6 $M_\odot$, 400 $M_\odot$ pc^{-2}) at t = 2.5 (1.0 $t_{\rm ff}$), 3.2 (1.3 $t_{\rm ff}$), 3.7 (1.5 $t_{\rm ff}$) and 5.0 Myr(2 $t_{\rm ff}$). *Top:* [C II] emission map. The pink star represents the position of the center of gravity of the cluster, and the pink dashed circle corresponds the half-mass radius of the cluster, respectively. *Bottom:* The circularly averaged [C II] luminosity. The horizontal axis denotes the distance from the center of gravity of the cluster. The vertical dotted line indicates the half-mass radius of the cluster.

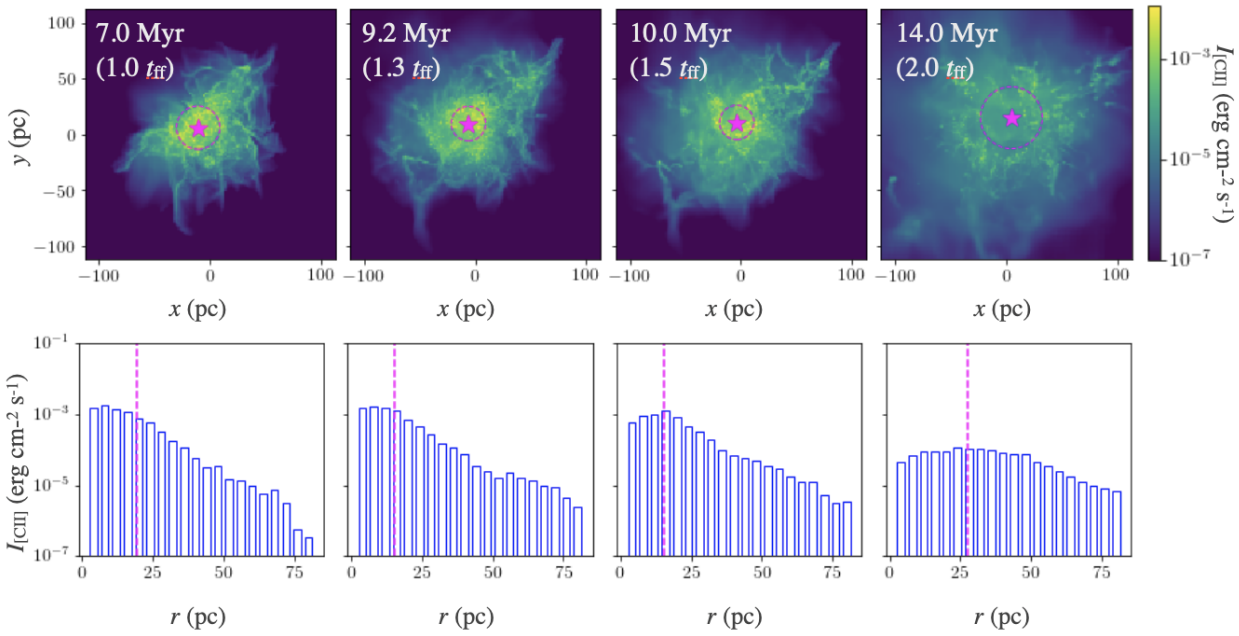

Figure 3.5: Same as Fig. 3.4, but for the case with ($M_{\rm cl}$, $\Sigma_{\rm cl}$) = (10^6 $M_\odot$, 100 $M_\odot$ pc^{-2}) at t = 7.0 (1.0 $t_{\rm ff}$), 9.2 (1.3 $t_{\rm ff}$), 10.0 (1.5 $t_{\rm ff}$) and 14.0 Myr(2 $t_{\rm ff}$).

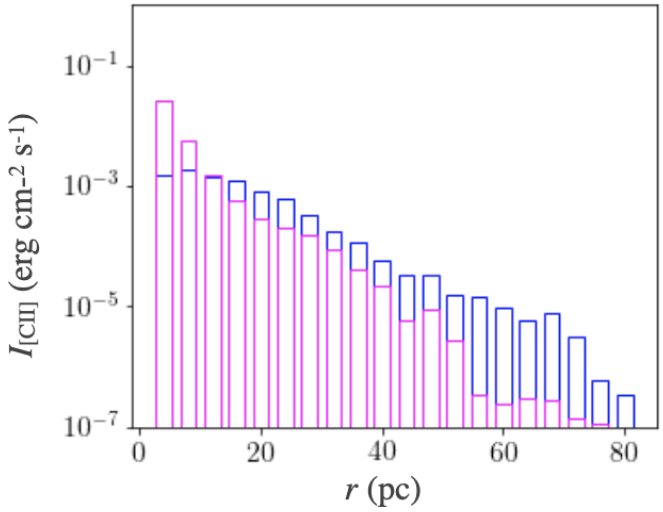

Figure 3.6: Radial profile of [C II] line emission maps of the cloud with ($M_{\rm cl}$, $\Sigma_{\rm cl}$) = (10^6 M$_\odot$, 400 M$_\odot$ pc^{-2}) at 3.7 Myr (1.5 $t_{\rm ff}$) (pink) and cloud with ($M_{\rm cl}$, $\Sigma_{\rm cl}$) = (10^6 M$_\odot$, 100 M$_\odot$ pc^{-2}) at t = 7.0 Myr (1.0 $t_{\rm ff}$) (blue). Star formation undergoes actively in both case.

Chapter 4

Conclusions

We have developed a semi-analytic model to investigate the FUV feedback on molecular clouds, particularly effects on the thermal and chemical states of the irradiated gas. On the basis of the previous model by Kim et al. (2016), we have solved the thermal and chemical structure of the PDR as well as the dynamical expansion of an H II region assuming spherical symmetry. We have first evaluated the impacts of the FUV feedback on the resulting minimum SFEs supposing that the star formation is suppressed in the warm PDR where the temperature is more than a threshold value, i.e., ~ 100 K. We have also calculated the chemical composition of the gas that is not converted to stars, i.e., the cloud remnants, under the FUV radiation from the newborn star cluster.

Following Kim et al. (2016), we have calculated the minimum SFEs as functions of the cloud surface density $\Sigma_{\rm cl}$ for different cloud masses of $M_{\rm cl} = 10^4, 10^5, 10^6$ $M_\odot$. We argue that the FUV feedback is more effective than the pure EUV feedback caused only by the expansion of the H II regions, particularly for massive clouds with $M_{\rm cl} > 10^5$ $M_\odot$ and with the low surface density, $\Sigma_{\rm cl} < 100$ $M_\odot$ pc^{-2}. The minimum SFEs are reduced by the FUV feedback by no less than an order of magnitude when the star formation is assumed to be suppressed above the threshold temperature, 100 K. A key quantity to interpret such dependencies is the FUV flux at the cloud edge $r = R_{\rm cl}$ when the cloud is assumed to be disrupted by the EUV feedback, $G_{\rm out}$. If $G_{\rm out}$ is large enough, it means that the cloud is sufficiently heated up by the FUV radiation before the EUV feedback operates, suggesting that the minimum SFE is predominantly determined by the FUV feedback. Our analyses show the scaling relation $G_{\rm out} \propto M_{\rm cl}^{1/2}\Sigma_{\rm cl}^{7/2}$, which explains why the FUV feedback is more effective with the higher $M_{\rm cl}$. The same scaling suggests that $G_{\rm out}$ is rather smaller with the lower $\Sigma_{\rm cl}$ for a given cloud mass $M_{\rm cl}$, which apparently contradicts with the trend that the FUV feedback is more effective for the lower $\Sigma_{\rm cl}$. The discrepancy is explained by the fact that the [C II] line cooling, the dominant process, becomes inefficient sharply with decreasing $\Sigma_{\rm cl}$ (or the volume density for a fixed $M_{\rm cl}$). Owing to this, the cloud gas tends to be easily heated up even by the weak FUV radiation field. Therefore, the minimum SFE is limited primarily by the FUV feedback with the lower $\Sigma_{\rm cl}$.

Moreover, our analyses on the chemical compositions of the cloud remnants suggest that a large part of them are actually "CO-dark", except for the cases with $M_{\rm cl} = 10^4$ $M_\odot$ and $\Sigma_{\rm cl} > 300$ $M_\odot$ pc^{-2}. This is because the column densities of the cloud remnants are $2 - 7 \times 10^{21}$ cm^{-2} with the wide range of parameters $M_{\rm cl}$ and $\Sigma_{\rm cl}$. With such small column densities

corresponding to $A_V \simeq$ a few, CO molecules within the cloud remnants are not protected against the incident FUV radiation by the dust attenuation. Only hydrogen molecules survive with the efficient self-shielding effect by contrast. We have also confirmed that such a feature should be the same even for cases where the minimum SFE is primarily limited by the EUV feedback, i.e., where the stellar FUV radiation only plays a minor role in destroying the natal clouds. The dispersed molecular clouds are potential factories of the CO-dark gas, which returns into the cycle of the interstellar medium (Chapter 2).

Also, we have examined the observational signatures of the cloud forming a YMC. We calculated the line emissions such as [C II], [O I], and CO, and the line-of-sight velocity of the molecular gas on the near side of the cluster based on the two cases where YMC forms or not in 3D RHD simulation performed by Fukushima & Yajima (2021). We analyzed the results of two simulations for initial cloud mass $M_{\rm cl} = 10^6$ $M_\odot$: one with YMC-formation ("Compact model", surface density $\Sigma_{\rm cl} = 400$ $M_\odot$ pc^{-2}, free-fall time $t_{\rm ff} \sim 2.5$ Myr), and the other without YMC-formation ("Diffuse model", $\Sigma_{\rm cl} = 100$ $M_\odot$ pc^{-2}, $t_{\rm ff} \sim 7$ Myr). A notable difference in the evolutionary process between the two models is whether active star formation continues after ~ 1.5 $t_{\rm ff}$ or not. In both models, infall motion (~ 2 km/s) of molecular gas within ~ 20 pc around the cluster is seen in the star-forming phase. In the Diffuse model, the feature is only observed in the first ~ 1 $t_{\rm ff}$, but in the Compact model, infall motion can be observed continuously even after ~ 1.5 $t_{\rm ff}$. We also found that the Compact model tends to have stronger line emission in the center of the cluster and a steeper radial profile than the Diffuse model. In short, we suppose that YMC-forming clouds can demonstrate the infall motion of molecular gas into the ionized region and the highly concentrated line emission in observations (Chapter 3).

Appendix A

Radial distributions of [O I] and CO line emission around the cluster

We discussed the properties of [C II] line emission map and its radial profile in Section 3.3.2. In addition, we have also performed similar calculations for [O I] and CO lines. In this Appendix, we present the results of these calculations. Figs. A.1 - A.4 show the line emission map and its averaged radial profiles. These are the same figures as Figs. 3.4 and3.5, but for [O I] and CO lines.

First we look into the [O I] emission. Figs. A.1 and A.2 show the time evolution of [O I] emission map and its radial profile in Compact and Diffuse model. [O I] line corresponds only the distribution of neutral gas, so its emission map has more characteristics signatures. Especially in Diffuse model (Fig. A.2), the [O I] emission is reduced in cluster center region. This is because the neutral gases are disrupted by outflow driven by photoionization feedback.

Next, we investigate the CO emission. Figs. A.3 and A.4 show the time evolution of [CO] emission map and its radial profile in Compact and Diffuse model. In the Compact model (Fig. A.3), the CO line emission remains throughout the evolution. In particular, the core-like structure becomes more pronounced after $t \sim 1.3\ t_{\rm ff}$. The CO line emission remains strong only exclusively near the center at $2.0\ t_{\rm ff}$. In the Diffuse model (Fig. A.3), on the other hand, although CO emission can be seen at $1.0\ t_{\rm ff}$, the core structure does not remain as in the Compact model as it evolves, and CO emission is almost invisible at $2.0\ t_{\rm ff}$. This is due to the destruction of CO molecules by radiation feedback.

We also compare the radial profile of the [CO] emission at the snapshots where there is the infall motion toward the cluster center. Fig. A.5 compares the radial profile of the CO emission in the Compact model at $t = 1.5\ t_{\rm ff}$ and that in the Diffuse model at $t = 1.0\ t_{\rm ff}$. We see the substantial excess of the CO central peak emission in Compact model in comparison to the Diffuse model. Such a difference is more remarkable than that of the [C II] emission presented in Fig. 3.6.

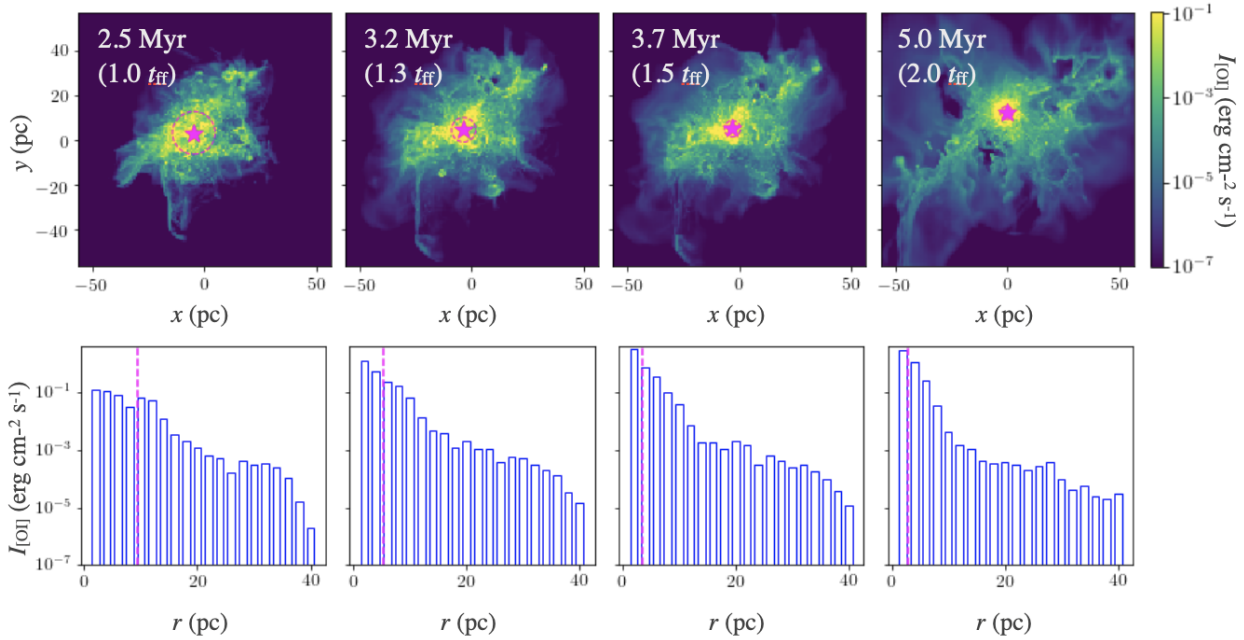

Figure A.1: Same as Fig. 3.4, but for the [O I] emission of the cloud with ($M_{\rm cl}$, $\Sigma_{\rm cl}$) = (10^6 $M_\odot$, 400 $M_\odot$ pc^{-2}) at t = 2.5 (1.0 $t_{\rm ff}$), 3.2 (1.3 $t_{\rm ff}$), 3.7 (1.5 $t_{\rm ff}$) and 5.0 Myr(2 $t_{\rm ff}$).

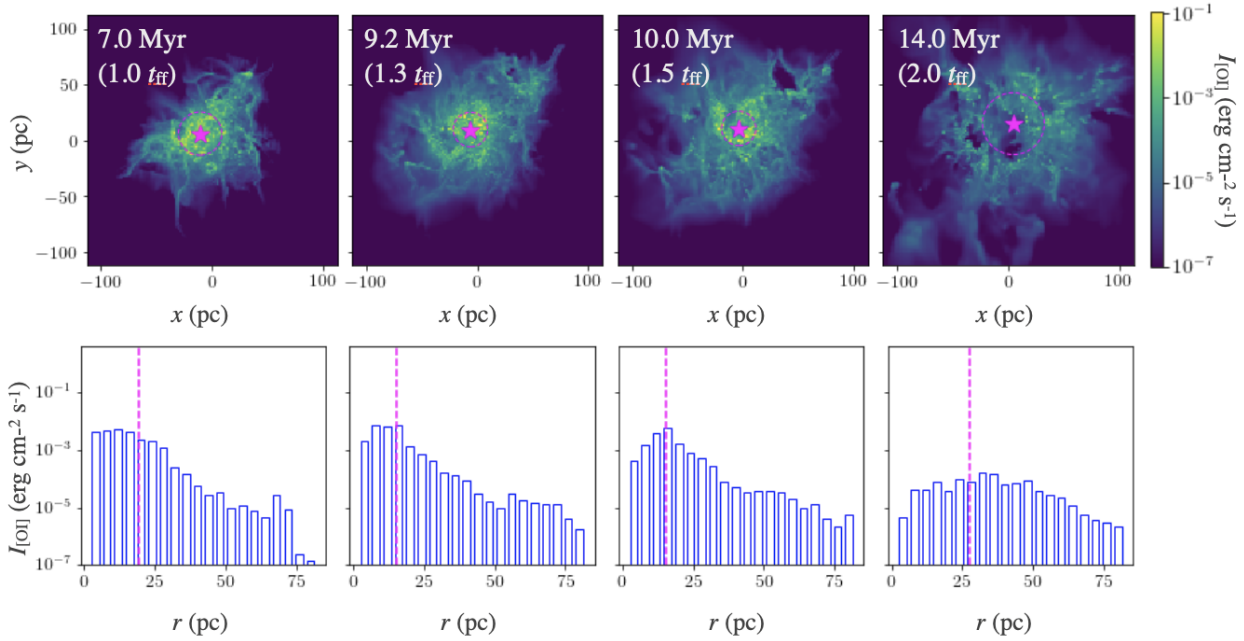

Figure A.2: Same as Fig. A.1, but for the case with ($M_{\rm cl}$, $\Sigma_{\rm cl}$) = (10^6 $M_\odot$, 100 $M_\odot$ pc^{-2}) at t = 7.0 (1.0 $t_{\rm ff}$), 9.2 (1.3 $t_{\rm ff}$), 10.0 (1.5 $t_{\rm ff}$) and 14.0 Myr(2 $t_{\rm ff}$).

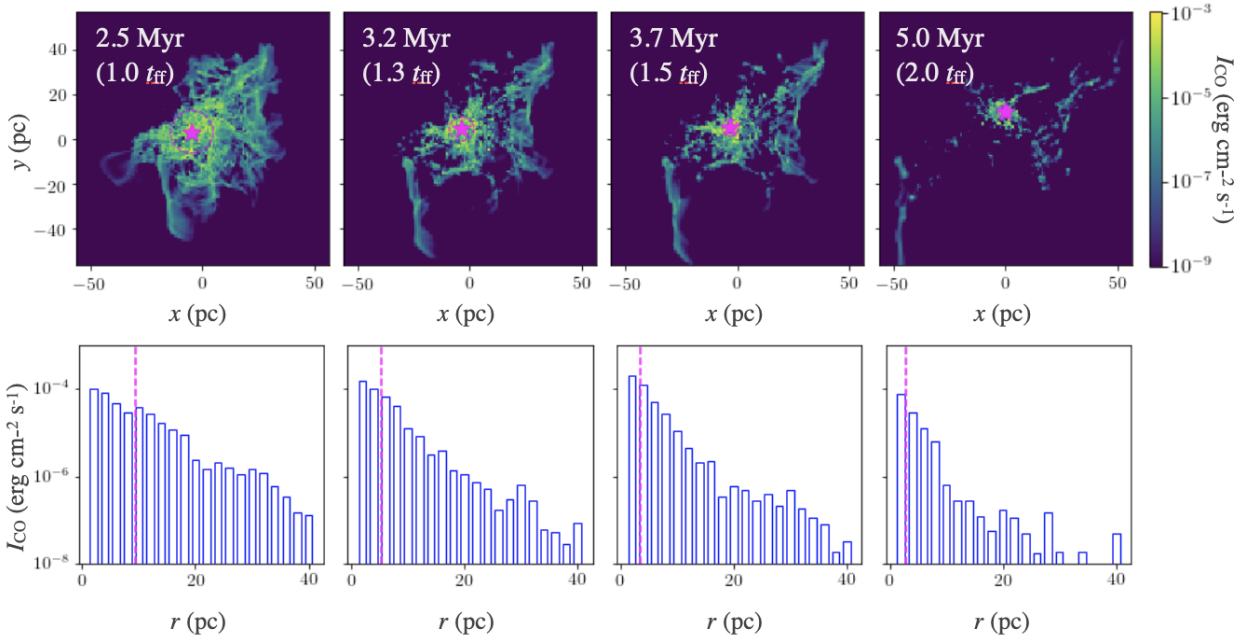

Figure A.3: Same as Fig. 3.4, but for the CO(1-0) emission of the cloud with ($M_{\rm cl}$, $\Sigma_{\rm cl}$) = (10^6 M$_\odot$, 400 M$_\odot$ pc^{-2}) at t = 2.5 (1.0 $t_{\rm ff}$), 3.2 (1.3 $t_{\rm ff}$), 3.7 (1.5 $t_{\rm ff}$) and 5.0 Myr(2 $t_{\rm ff}$).

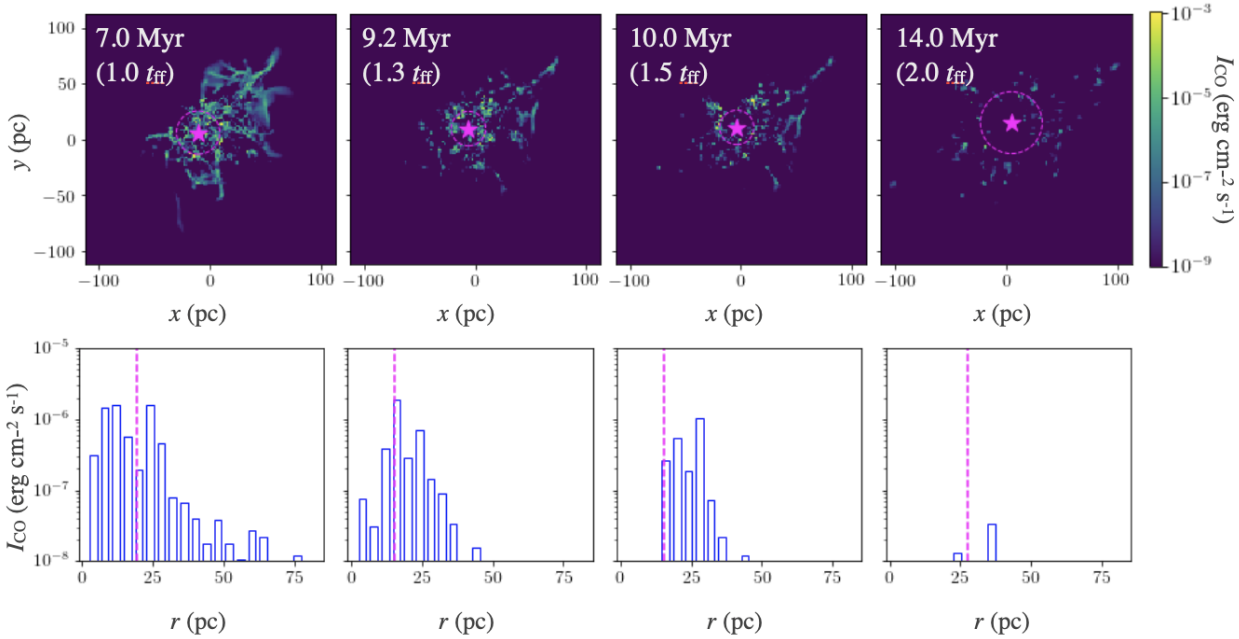

Figure A.4: Same as Fig. A.3, but for the case with ($M_{\rm cl}$, $\Sigma_{\rm cl}$) = (10^6 M$_\odot$, 100 M$_\odot$ pc^{-2}) at t = 7.0 (1.0 $t_{\rm ff}$), 9.2 (1.3 $t_{\rm ff}$), 10.0 (1.5 $t_{\rm ff}$) and 14.0 Myr(2 $t_{\rm ff}$).

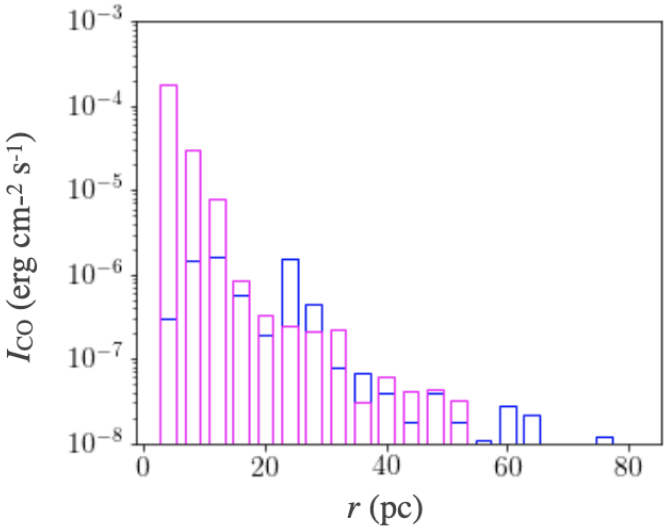

Figure A.5: Same as Fig. 3.6, but for the CO(1-0) emission.

Acknowledgements

I would like to express my heartfelt gratitude to my supervisors, Profs. Shin Mineshige and Takashi Hosokawa provided me with elaborated guidance, considerable encouragement, and invaluable discussion that make my research of great achievement.

I sincerely thank Dr. Jeong-Gyu Kim for helpful discussions and comments on the manuscript as co-author of my publication (Inoguchi et al. 2020). I would also like to thank Dr. Shuichiro Inutsuka for fruitful discussions and comments in the preparation of my publication.

I am grateful to Dr. Pedro Palmeirim for providing me with the observational data we argued in Section 2.3.5.

I would like to thank Dr. Hajime Fukushima for collaboration in my studies described in Chapter 3.

Reference

Arthur S. J., Henney W. J., Mellema G., de Colle F., Vázquez-Semadeni E., 2011, Monthly Notices of the Royal Astronomical Society, 414, 1747

Bakes E. L. O., Tielens A. G. G. M., 1994, Astrophysical Journal, 427, 822

Bisbas T. G., et al., 2015, Monthly Notices of the Royal Astronomical Society, 453, 1324

Bisbas T. G., van Dishoeck E. F., Papadopoulos P. P., Szűcs L., Bialy S., Zhang Z.-Y., 2017, Astrophysical Journal, 839, 90

Butler M. J., Tan J. C., Teyssier R., Rosdahl J., Van Loo S., Nickerson S., 2017, Astrophysical Journal, 841, 82

Cardelli J. A., Meyer D. M., Jura M., Savage B. D., 1996, Astrophysical Journal, 467, 334

Cartledge S. I. B., Lauroesch J. T., Meyer D. M., Sofia U. J., 2004, Astrophysical Journal, 613, 1037

Chabrier G., 2003, Publications of the Astronomical Society of the Pacific, 115, 763

Chen Y., Bressan A., Girardi L., Marigo P., Kong X., Lanza A., 2015, Monthly Notices of the Royal Astronomical Society, 452, 1068

Clark P. C., Glover S. C. O., Klessen R. S., Bonnell I. A., 2012, Monthly Notices of the Royal Astronomical Society, 424, 2599

Dale J. E., 2015, New Astronomy Review, 68, 1

Dale J. E., Ercolano B., Bonnell I. A., 2012, Monthly Notices of the Royal Astronomical Society, 424, 377

Diaz-Miller R. I., Franco J., Shore S. N., 1998, Astrophysical Journal, 501, 192

Draine B. T., 2011, Astrophysical Journal, 732, 100

Draine B. T., Bertoldi F., 1996, Astrophysical Journal, 468, 269

Fall S. M., Krumholz M. R., Matzner C. D., 2010, Astrophysical Journal, 710, L142

Federrath C., Banerjee R., Clark P. C., Klessen R. S., 2010, Astrophysical Journal, 713, 269

Forbes J. C., Krumholz M. R., Goldbaum N. J., Dekel A., 2016, Nature, 535, 523

Franco J., Tenorio-Tagle G., Bodenheimer P., 1990, Astrophysical Journal, 349, 126

Fukui Y., Kawamura A., 2010, Annual Review of Astronomy and Astrophysics, 48, 547

Fukushima H., Yajima H., 2021, Monthly Notices of the Royal Astronomical Society, 506, 5512

Fukushima H., Hosokawa T., Chiaki G., Omukai K., Yoshida N., Kuiper R., 2020a, Monthly Notices of the Royal Astronomical Society, 497, 829

Fukushima H., Yajima H., Sugimura K., Hosokawa T., Omukai K., Matsumoto T., 2020b, Monthly Notices of the Royal Astronomical Society, 3845, 3830

Gaches B. A. L., Offner S. S. R., 2018, Astrophysical Journal, 854, 156

Gavagnin E., Bleuler A., Rosdahl J., Teyssier R., 2017, Monthly Notices of the Royal Astronomical Society, 472, 4155

Geen S., Hennebelle P., Tremblin P., Rosdahl J., 2015, Monthly Notices of the Royal Astronomical Society, 454, 4484

Geen S., Pellegrini E., Bieri R., Klessen R., 2019, arXiv e-prints, p. arXiv:1906.05649

Gong H., Ostriker E. C., 2013, Astrophysical Journal, Supplement, 204, 8

Gong M., Ostriker E. C., Kim C.-G., 2018, Astrophysical Journal, 858, 16

González-Samaniego A., Vazquez-Semadeni E., 2020, arXiv e-prints, p. arXiv:2003.12711

Gorti U., Hollenbach D., 2002, Astrophysical Journal, 573, 215

Grenier I. A., Kaufman Bernadó M. M., Romero G. E., 2005, Astrophysics and Space Science, 297, 109

Habing H. J., 1968, Bulletin Astronomical Institute of the Netherlands, 19, 421

Haid S., Walch S., Seifried D., Wünsch R., Dinnbier F., Naab T., 2019, Monthly Notices of the Royal Astronomical Society, 482, 4062

Haworth T. J., Harries T. J., Acreman D. M., Bisbas T. G., 2015, Monthly Notices of the Royal Astronomical Society, 453, 2277

He C.-C., Ricotti M., Geen S., 2019, arXiv e-prints, p. arXiv:1904.07889

Hollenbach D., McKee C. F., 1979, Astrophysical Journal, Supplement, 41, 555

Hollenbach D., McKee C. F., 1989, Astrophysical Journal, 342, 306

Hollenbach D. J., Tielens A. G. G. M., 1999, Reviews of Modern Physics, 71, 173

Hosokawa T., 2007, Astronomy and Astrophysics, 463, 187

Hosokawa T., Inutsuka S.-i., 2006, Astrophysical Journal, 646, 240

Hosokawa T., Inutsuka S.-i., 2007, Astrophysical Journal, 664, 363

Howard C. S., Pudritz R. E., Harris W. E., 2016, Monthly Notices of the Royal Astronomical Society, 461, 2953

Hu C.-Y., Naab T., Glover S. C. O., Walch S., Clark P. C., 2017, Monthly Notices of the Royal Astronomical Society, 471, 2151

Inoguchi M., Hosokawa T., Mineshige S., Kim J.-g., 2020, Monthly Notices of the Royal Astronomical Society, 497, 5061

Inoue T., Inutsuka S.-i., 2008, Astrophysical Journal, 687, 303

Inoue T., Inutsuka S.-i., 2009, Astrophysical Journal, 704, 161

Inutsuka S.-i., Inoue T., Iwasaki K., Hosokawa T., 2015, Astronomy and Astrophysics, 580, A49

Ishiki S., Okamoto T., 2017, Monthly Notices of the Royal Astronomical Society, 466, L123

Kennicutt R. C., Evans N. J., 2012, Annual Review of Astronomy and Astrophysics, 50, 531

Kim J.-G., Kim W.-T., Ostriker E. C., 2016, Astrophysical Journal, 819, 137

Kim J.-G., Kim W.-T., Ostriker E. C., Skinner M. A., 2017, Astrophysical Journal, 851, 93

Kim J.-G., Kim W.-T., Ostriker E. C., 2018, Astrophysical Journal, 859, 68

Koyama H., Inutsuka S.-I., 2000, Astrophysical Journal, 532, 980

Kruijssen J. M. D., et al., 2019, Nature, 569, 519

Krumholz M. R., Matzner C. D., 2009, Astrophysical Journal, 703, 1352

Krumholz M. R., Fumagalli M., da Silva R. L., Rendahl T., Parra J., 2015, Monthly Notices of the Royal Astronomical Society, 452, 1447

Krumholz M. R., McKee C. F., Bland -Hawthorn J., 2019, Annual Review of Astronomy and Astrophysics, 57, 227

Lada C. J., Lada E. A., 2003, Annual Review of Astronomy and Astrophysics, 41, 57

Langer W., 1976, Astrophysical Journal, 206, 699

Lee E. J., Miville-Deschênes M.-A., Murray N. W., 2016, Astrophysical Journal, 833, 229

Li Q., Narayanan D., Davè R., Krumholz M. R., 2018, Astrophysical Journal, 869, 73

Lopez L. A., Krumholz M. R., Bolatto A. D., Prochaska J. X., Ramirez-Ruiz E., Castro D., 2014, Astrophysical Journal, 795, 121

Matsumoto T., Dobashi K., Shimoikura T., 2015, Astrophysical Journal, 801, 77

Matzner C. D., 2002, Astrophysical Journal, 566, 302

McKee C. F., Storey J. W. V., Watson D. M., Green S., 1982, Astrophysical Journal, 259, 647

McKee C. F., van Buren D., Lazareff B., 1984, Astrophysical Journal, Letters, 278, L115

Mellema G., Arthur S. J., Henney W. J., Iliev I. T., Shapiro P. R., 2006, Astrophysical Journal, 647, 397

Murray N., Quataert E., Thompson T. A., 2010, Astrophysical Journal, 709, 191

Naab T., Ostriker J. P., 2017, Annual Review of Astronomy and Astrophysics, 55, 59

Nakatani R., Yoshida N., 2018, arXiv e-prints, p. arXiv:1811.00297

Nelson R. P., Langer W. D., 1997, Astrophysical Journal, 482, 796

Nelson R. P., Langer W. D., 1999, Astrophysical Journal, 524, 923

Omukai K., Nishi R., 1998, Astrophysical Journal, 508, 141

Osterbrock D. E., 1989, Sky and Telescope, 78, 491

Palmeirim P., et al., 2017, Astronomy and Astrophysics, 605, A35

Peters T., et al., 2017, Monthly Notices of the Royal Astronomical Society, 466, 3293

Pineda J. L., Langer W. D., Velusamy T., Goldsmith P. F., 2013, Astronomy and Astrophysics, 554, A103

Pineda J. L., Langer W. D., Goldsmith P. F., 2014, Astronomy and Astrophysics, 570, A121

Planck Collaboration et al., 2011, Astronomy and Astrophysics, 536, A21

Portegies Zwart S. F., McMillan S. L. W., Gieles M., 2010, Annual Review of Astronomy and Astrophysics, 48, 431

Rahner D., Pellegrini E. W., Glover S. C. O., Klessen R. S., 2017, Monthly Notices of the Royal Astronomical Society, 470, 4453

Rahner D., Pellegrini E. W., Glover S. C. O., Klessen R. S., 2019, Monthly Notices of the Royal Astronomical Society, 483, 2547

Raskutti S., Ostriker E. C., Skinner M. A., 2016, Astrophysical Journal, 829, 130

Raskutti S., Ostriker E. C., Skinner M. A., 2017, Astrophysical Journal, 850, 112

Roger R. S., Dewdney P. E., 1992, Astrophysical Journal, 385, 536

Rogers H., Pittard J. M., 2013, Monthly Notices of the Royal Astronomical Society, 431, 1337

Seifried D., Haid S., Walch S., Borchert E. M., Bisbas T. G., 2019, arXiv e-prints, p. arXiv:1906.01015

Smith R. J., Glover S. C. O., Klessen R. S., 2014, Monthly Notices of the Royal Astronomical Society, 445, 2900

Sollins P. K., Zhang Q., Keto E., Ho P. T. P., 2005, Astrophysical Journal, Letters, 624, L49

Spitzer L., 1978, Physical processes in the interstellar medium, doi:10.1002/9783527617722.

Tan J. C., Beltrán M. T., Caselli P., Fontani F., Fuente A., Krumholz M. R., McKee C. F., Stolte A., 2014, in Beuther H., Klessen R. S., Dullemond C. P., Henning T., eds, Protostars and Planets VI. p. 149 (arXiv:1402.0919), doi:10.2458/azu˙uapress˙9780816531240-ch007

Tenorio-Tagle G., 1979, Astronomy and Astrophysics, 71, 59

Thompson T. A., Krumholz M. R., 2016, Monthly Notices of the Royal Astronomical Society, 455, 334

Tielens A. G. G. M., Hollenbach D., 1985, Astrophysical Journal, 291, 722

Walch S. K., Whitworth A. P., Bisbas T., Wünsch R., Hubber D., 2012, Monthly Notices of the Royal Astronomical Society, 427, 625

Walch S., Whitworth A. P., Bisbas T. G., Wünsch R., Hubber D. A., 2013, Monthly Notices of the Royal Astronomical Society, 435, 917

Walch S., Whitworth A. P., Bisbas T. G., Hubber D. A., Wünsch R., 2015, Monthly Notices of the Royal Astronomical Society, 452, 2794

Weaver R., McCray R., Castor J., Shapiro P., Moore R., 1977, Astrophysical Journal, 218, 377

Whitworth A., 1979, Monthly Notices of the Royal Astronomical Society, 186, 59

Williams J. P., McKee C. F., 1997, Astrophysical Journal, 476, 166

Williams R. J. R., Bisbas T. G., Haworth T. J., Mackey J., 2018, Monthly Notices of the Royal Astronomical Society, 479, 2016

Wolfire M. G., Hollenbach D., McKee C. F., Tielens A. G. G. M., Bakes E. L. O., 1995, Astrophysical Journal, 443, 152

Wolfire M. G., Hollenbach D., McKee C. F., 2010, Astrophysical Journal, 716, 1191

Yorke H. W., 1986, Annual Review of Astronomy and Astrophysics, 24, 49

van Dishoeck E. F., 1992, in Singh P. D., ed., IAU Symposium Vol. 150, Astrochemistry of Cosmic Phenomena. p. 143

van Dishoeck E. F., Black J. H., 1988, Astrophysical Journal, 334, 771